Intracellular Ca^{2+} channels initiate physiological glucose signaling in beta cells examined *in situ*

Sandra Postić[1*], Srdjan Sarikas[1*], Johannes Pfabe[1], Viljem Pohorec[2], Lidija Križančić Bombek[2], Nastja Sluga[2], Maša Skelin Klemen[2], Jurij Dolenšek[2], Dean Korošak[2], Andraž Stožer[2], Carmella Evans-Molina[3,4], James D Johnson[5], Marjan Slak Rupnik[1,2,6**]

[1] Center for physiology and pharmacology, Medical University of Vienna, Vienna, Austria
[2] Institute of Physiology, Faculty of Medicine, University of Maribor, Slovenia
[3] Center for Diabetes and Metabolic Diseases and the Herman B Wells Center for Pediatric Research, Indiana University School of Medicine, Indianapolis, Indiana
[4] Richard L. Roudebush VA Medical Center, Indianapolis, Indiana
[5] Diabetes Research Group, Life Sciences Institute, Department of Cellular and Physiological Sciences, University of British Columbia, Vancouver, Canada
[6] Alma Mater Europaea – European Center Maribor, Maribor, Slovenia

*These authors contributed equally to this work.

For correspondence: **marjan.slakrupnik@meduniwien.ac.at
Marjan Slak Rupnik, Center for physiology and pharmacology, Medical University of Vienna, Schwarzspanierstrasse 17, 1090 Vienna, Austria, phone: (+43) 1 40160 31113

Short title: Intracellular Ca^{2+} release channels in beta cells
Keywords: insulin secretion, pancreatic slice islet recordings, ryanodine receptor, IP_3 receptor, endoplasmic reticulum

Abstract

Objective
Insulin release from pancreatic beta cells is driven by cytosolic $[Ca^{2+}]_c$ oscillations of several different time scales that are primarily attributed to plasma membrane ion channel activity. However, the majority of past studies have been performed at supraphysiological glucose concentrations above 10 mM using electrophysiologic approaches that solely measure plasma membrane ion fluxes. The role of endoplasmic reticulum (ER) Ca^{2+} stores in glucose-stimulated Ca^{2+} signaling remains poorly understood.
Methods
In this study, we hypothesized new, brighter $[Ca^{2+}]_c$ sensors coupled with high-resolution functional Ca^{2+} imaging could be used to test a previously unappreciated role for the ryanodine and IP_3 intracellular Ca^{2+} release channels in $[Ca^{2+}]_c$ oscillations stimulated by increases from 6 mM to 8 mM glucose.
Results
Using mouse pancreas tissue slices exposed to physiological glucose increments, our results show that glucose-dependent activation of IP_3 and ryanodine receptors produces two kinetically distinct forms of compound events involving calcium-induced Ca^{2+} release. Ca^{2+} release mediated by IP_3 and ryanodine receptors was sufficient to

generate Ca^{2+} oscillations and necessary for the response to physiological glucose, which could be initiated in the absence of Ca^{2+} influx across the plasma membrane through voltage-gated Ca^{2+} channels.
Conclusions
In aggregate, these data suggest that intracellular Ca^{2+} receptors play a key role in shaping glucose-dependent $[Ca^{2+}]_c$ responses in pancreatic beta cells *in situ*. In our revised model, the primary role for plasma membrane Ca^{2+} influx at physiological glucose concentrations is to refill ER Ca^{2+} stores.

1 Introduction

Decades of electrophysiological experiments on pancreatic beta cells have established a critical role for plasma membrane ion channels in controlling excitability, cytosolic Ca^{2+} fluctuations and insulin exocytosis [4, 54]. In typical electrophysiology experiments, beta cells are kept at 3 mM glucose where they are electrically silent, after which they are activated by an instantaneous stepwise increase to glucose levels well in excess of 10 mM [62]. Based on the results of these types of experiments, it is generally accepted in the field that such high glucose exposure stimulates insulin release via the following series of events. Glucose entry into the beta cells through glucose transporters leads to metabolic production of ATP, closure of the ATP-sensitive K^+ channels (K_{ATP} channels), followed by plasma membrane depolarization reaching the threshold for voltage-activated Ca^{2+} channels (VACCs), to trigger the diffusion of Ca^{2+} ions into the cytosol. This ultimately results in a complex spatio-temporal pattern of membrane potential depolarizations, $[Ca^{2+}]_c$ oscillations, and insulin vesicle exocytosis [15, 54, 59]. There is growing evidence that intracellular Ca^{2+} release channels, namely the IP_3 receptors (IP_3R) and the ryanodine receptors (RYR), contribute to Ca^{2+}-dependent insulin release in beta cells [20, 46, 47, 56]. However, their exact role in physiological activation of beta cells is not clear [54]. Moreover, multiple studies suggest that disturbed activity of intracellular Ca^{2+} release channels may contribute to beta cell dysfunction and glucose intolerance [42, 57, 74].

Assessing Ca^{2+} release from intracellular Ca^{2+} channels requires high temporal resolution recording. To date, single-cell recording of electrophysiological parameters during glucose-dependent depolarization has been accepted as the gold standard approach to assess the function of beta cells in islets at a millisecond time scale [15, 55]. Until recently, measurements of $[Ca^{2+}]_c$ oscillations were typically orders of magnitude slower than this required temporal resolution [45]. Fast and long-term recording of $[Ca^{2+}]_c$ oscillations was limited due to relatively weak fluorescence signal of the classical fluorophores, their high affinity Ca^{2+} binding that yielded phase lags, slow sampling rates, and substantial bleaching [21, 65]. However, novel fluorescent Ca^{2+}-sensing dyes that overcome most of the aforementioned technical issues [48], used together with enhanced data analysis, have enabled quantitation of changes in cytosolic Ca^{2+} concentrations with millisecond temporal and high spatial resolution in many cells at the same time enabling repeated stimulations. With these tools at hand, we conducted studies to revisit glucose-dependent beta cell activation and to test the contribution of IP_3 and RYR intracellular Ca^{2+} release channels during this activation.

2 Results

2.1 Imaging of beta cell $[Ca^{2+}]_c$ in pancreas slices at physiological glucose concentration

Pancreas tissue slices offer the opportunity to study beta cells *in situ* (Figure 1A) and under conditions that more closely resemble *in vivo* physiology compared to isolated islets and dispersed islet cells [43]. At substimulatory glucose concentrations (6 mM), beta cells from adult mice exhibited a stable resting level of Ca^{2+}. From a baseline of 6 mM, a physiological stimulatory glucose concentration (8 mM) after a typical delay of solution exchange and glucose metabolism, triggered a biphasic $[Ca^{2+}]_c$ pattern (Figure 1B,F). This initial increase in $[Ca^{2+}]_c$ has been previously termed the transient or asynchronous phase (Figure 1F, dark blue rectangles), followed by a prolonged plateau phase (Figure 1F, light blue dashed rectangles) [65, 66]. In both phases, we detected $[Ca^{2+}]_c$ oscillations at different time scales, spanning from millisecond to a hundred of second range (Figure 1CD). These $[Ca^{2+}]_c$ oscillations show elements of self-similarity as longer events were a temporal summation of series of shorter events, a feature that could be indicative of calcium-induced Ca^{2+} release-like (CICR) behavior (Figure 1).

During the initial transient phase, additionally characterizable with sizable delays between the activation of individual beta cell groups within an islet (Figure 1B), we recorded one or more large transient Ca^{2+} waves with a mean duration of tens of seconds with (Figure 1E(*)) or without discernible superimposed faster $[Ca^{2+}]_c$ oscillations (Figure 3E). When discernible, these faster events were often synchronized within clusters of beta cells in an islet. The large transient events were also occasionally recorded outside the transient phase (Figure 1B). In less than 30 % of recorded islets or in a small fraction of the cells in a typical islet, slow oscillations were more prominent and were apparent in both transient as well as in plateau phase (Figure 1B).

On the other hand, during the plateau phase we recorded mostly $[Ca^{2+}]_c$ oscillations with a mean halfwidth duration of a few seconds (Figure 1E(**)), occasionally exhibiting temporal summation as slowly rising and decaying slow changes (Figs. 1B,F). These events present a dominant scale in the control experiment at 8 mM glucose (Figure 1C). The fast oscillations within the plateau phase were typically well synchronized among the beta cells in an islet (Figs. 1B,D,F). The $[Ca^{2+}]_c$ oscillations during the plateau phase were also regenerative and could be stably recorded for hours at physiological glucose concentrations [25]. Due to the regenerative nature of the fast $[Ca^{2+}]_c$ events, we could design a triple stimulation protocol to be used on the same slice (Figure 1B). In this protocol, the initial period tested the responsiveness to the stimulation with 8 mM glucose (section 1), the second phase tested the effect of a specific pharmacological treatment during stimulation with 8 mM glucose (section 2) and the last phase characterized a washout period (section 3) (Figs. 2-4,7,8). The dynamic continuity of scales reflected in observed self-similarity did not allow reasonable use of classical statistical approaches to indicate significance in our data sets , which are typically not normally distributed. Using a Mann-Whitney Rank sum test, for example, uncovered a significant trend in the control triple experiment where halfwidth durations of the fast events increased with subsequent exposures to 8 mM glucose (Figure 1B). The median halfwidth increased from 2.4 s (Q1 1.7 s, Q3 3.1 s) during the first section of the protocol, 2.7 s (Q1 1.6 s, Q3 3.6 s) during the second section, and 2.9 s (Q1 1.5 s, Q3 4.2 s) for the third section, with the test p-value of about 10^{-9}. A similar comparison of the halfwidth durations of the slow events showed no statistical significance (p=0.467) between the stimulation periods). Additionally, detailed inspection of the fast $[Ca^{2+}]_c$ events in the plateau phase showed that they were

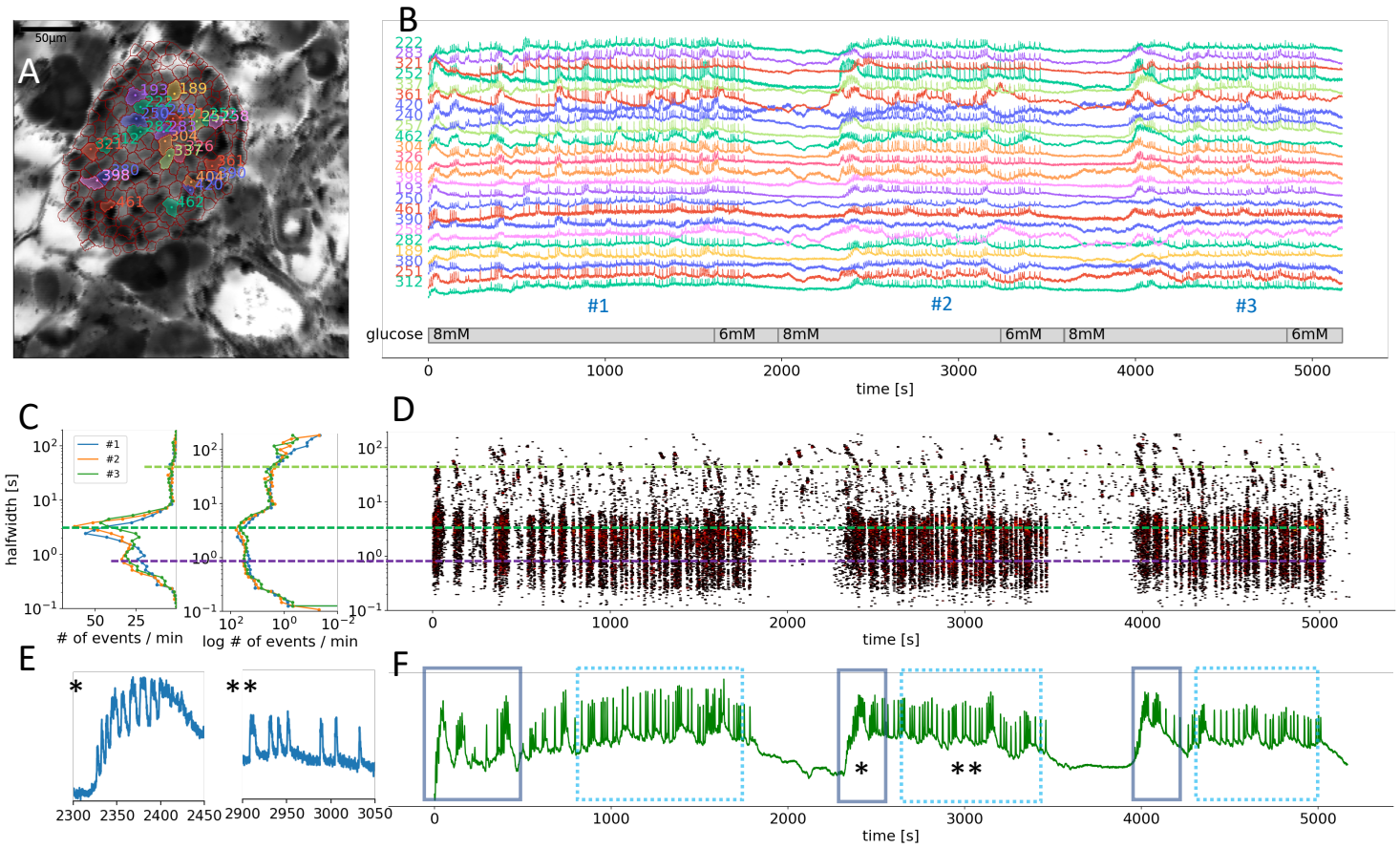

Figure 1. Time scales and heterogeneity of responses of $[Ca^{2+}]_c$ oscillations in mouse beta cells stimulated with a triple 8 mM glucose protocol. A, Calbryte 520 staining of a fresh tissue slice with labelled ROIs within the islet. **B**, Time course of the $[Ca^{2+}]_c$ changes in a selection of beta cells indicated in the panel A, exposed to a triple 8 mM glucose stimulation protocol. Individual treatment sections are numbered and indicated at the bottom **C**, Frequency histograms of the event halfwidth durations and **D**, onset time of the $[Ca^{2+}]_c$ events at all measured time scales. Note that the distribution of all major time scales was comparable between the three stimulation sections in the control experiments. The dominant time scale are the events with a halfwidth duration of 3-4 s (dark green). Both faster sub second (violet dashed line) and slower events (light green dashed line) were also observed **E**, Expanded time traces from a representative ROI indicating the a slow event from a transient phase (*) and a series of fast events during the plateau phase (**) as indicated in panel F. **F**, Time trace of the average of all ROIs in the presented islet (n=193). There is a prominent superposition of the fast activity on the plateau phases between the ROis.

compound events composed of even faster $[Ca^{2+}]_c$ oscillations with a mean halfwidth duration below one second (Figs. 2C, 4F). Similar millisecond events have been so far observed only as spikes on top of the bursts of the electrical activity, and have been designated as slow Ca^{2+} action potentials [4, 27, 32] mediated by the dominant contribution of L-type VACCs [58]. Our approach therefore offered insight into $[Ca^{2+}]_c$ events on times scales spanning several orders of magnitude (Figure 1C), with temporal resolution comparable to that achieved with electrophysiological approach, and with an upgrade of simultaneously visualizing the activity of all islet cells in an optical plane permitting the interrogation of a collective behavior *in situ*.

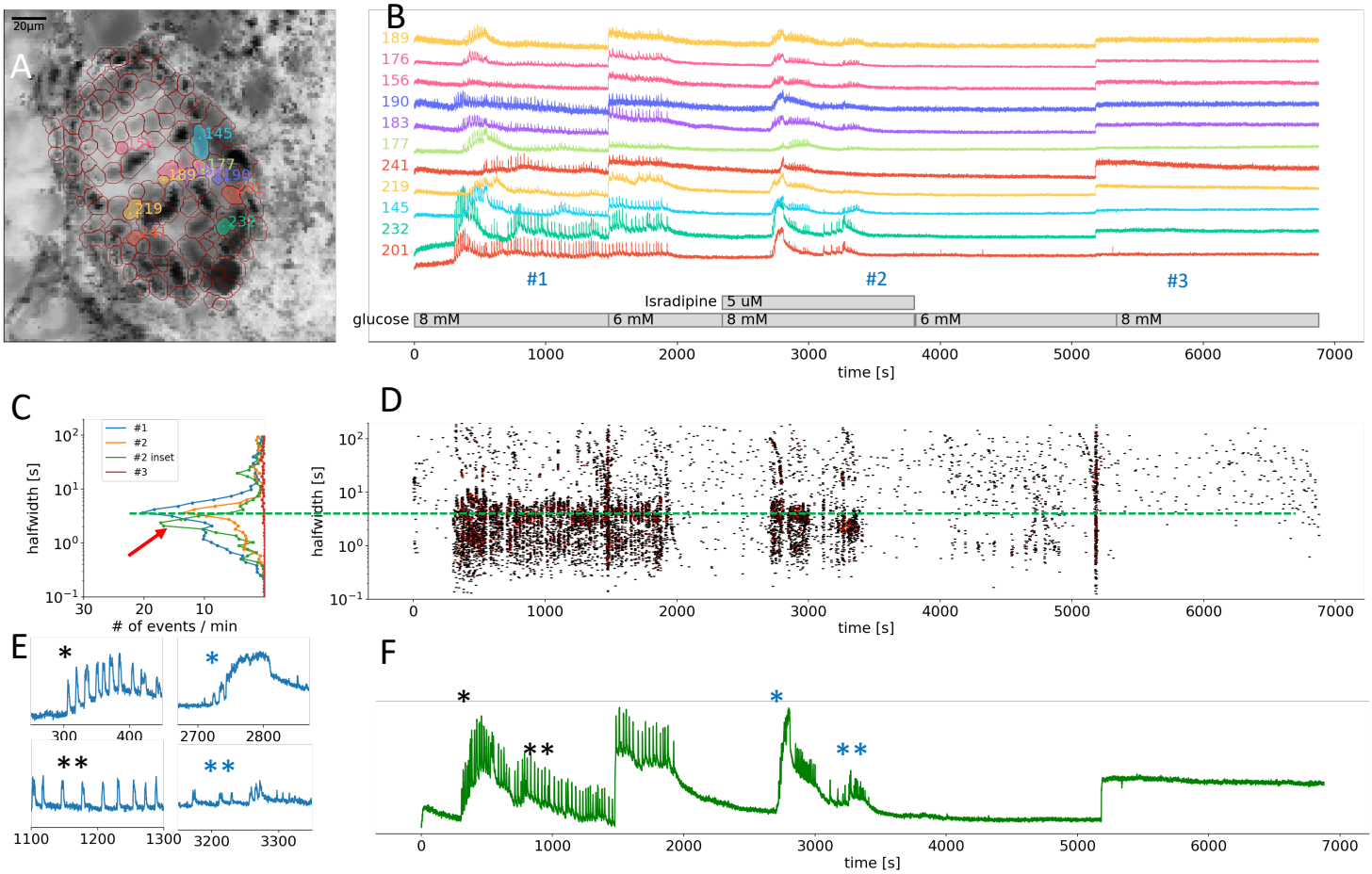

Figure 2. Glucose-dependent activation of beta cells in the absence of functional VACCs. **A**, Calbryte 520 staining of an islet in a fresh tissue slice. **B**, Time course of the $[Ca^{2+}]_c$ changes in a selection of beta cells indicated in the panel A, exposed to a triple 8 mM glucose stimulation protocol. Saturating concentration of isradipine (5 μM) was applied in the section 2 of the protocol. Abrupt vertical jumps in all traces show artefacts due to a passage of an air bubbles, which sometimes appear during the experiment. **C**, Frequency histograms of the event halfwidth durations and (**D**) onset time of the $[Ca^{2+}]_c$ events at all measured time scales. Note that the transient activation and the initiation of the plateau phase was comparable to control conditions, until the events shortened and then disappeared completely. **E**, Expanded time traces from a representative ROI indicating the a slow event from a transient phase (*) and plateau phase (**) as indicated in panel F. **F**, Time trace of the average of all ROIs in the presented islet (n=109). There is a prominent superposition of the fast activity on the plateau phases between the ROis. Asterisks from sections 1 and 2 are color coded.

2.2 $[Ca^{2+}]_c$ oscillations can be initiated during L-type VACC block

Our first step towards elucidating the molecular mechanisms of these Ca^{2+} signals was to define to what extent these multiple scales of $[Ca^{2+}]_c$ oscillations depended on L-type VACCs. Previous experiments performed on beta cell-selective Cav1.2 Ca^{2+} channel null mice showed that, in the absence of the Ca^{2+} channel, $[Ca^{2+}]_c$ oscillations were only moderately affected during the first minutes of the glucose stimulation, with a

characteristic change in bursting pattern observed during acute stimulation [58]. In the present study, we used the triple stimulation protocol to test the effect of a saturating concentration (5 μM) isradipine, a specific L-type VACC blocker (Figure 2). Consistent with the knockout mouse data, we observed a virtually intact transient phase and initial plateau activity with a halfwidth duration with a median value of 3.1 s (Q1 1.8 s, Q3 4.6 s) during the first section and 3.4 s (Q1 2.1 s, Q3 4.3s, p=0.249). in the continuation of the plateau phased the pattern of $[Ca^{2+}]_c$ oscillations was characterized by shortened events with the median value 2.4 s (Q1 1.9 s, Q3 3.1.s, $p<10^{-15}$)(Figure 2). Instead of CICR-like compound oscillations of the dominant time scale, a reduced number of events with a mean halfwidth duration around 1 second remained that could reflect progressively lower probability of CICR after blockage of VACCs towards isolated release events (Figure 2C). Within minutes after, the change in $[Ca^{2+}]_c$ oscillation pattern, the events disappeared completely, an effect that could not be washed out and recovered within the timeframe of the triple stimulation protocol (Figure 2). Longer washout period following exposure to dihydropyridine could recover the responsiveness to 8 mM glucose.

Blocking L-type VACCs with isradipine during the plateau phase produced a similar change in the phenotype of $[Ca^{2+}]_c$ oscillations before these subsided completely (Figure S2-1). We obtained a similar result when we prevented the depolarization using 100 μM diazoxide (Figure S2-2). At this concentration, diazoxide clamps the membrane potential close to the resting membrane potential, which is around the diffusion equilibrium potential for K^+ (E_K; -90 mV) [21, 76] and outside the range where VACCs could be activated [39]). Our experiments strongly support a role for L-type VACCs for the regenerative glucose-dependent activity of beta cells during the plateau phase [72]. However, we also confirmed previous observations that these channels play only a minor role during the first minutes of beta cells activation [53].

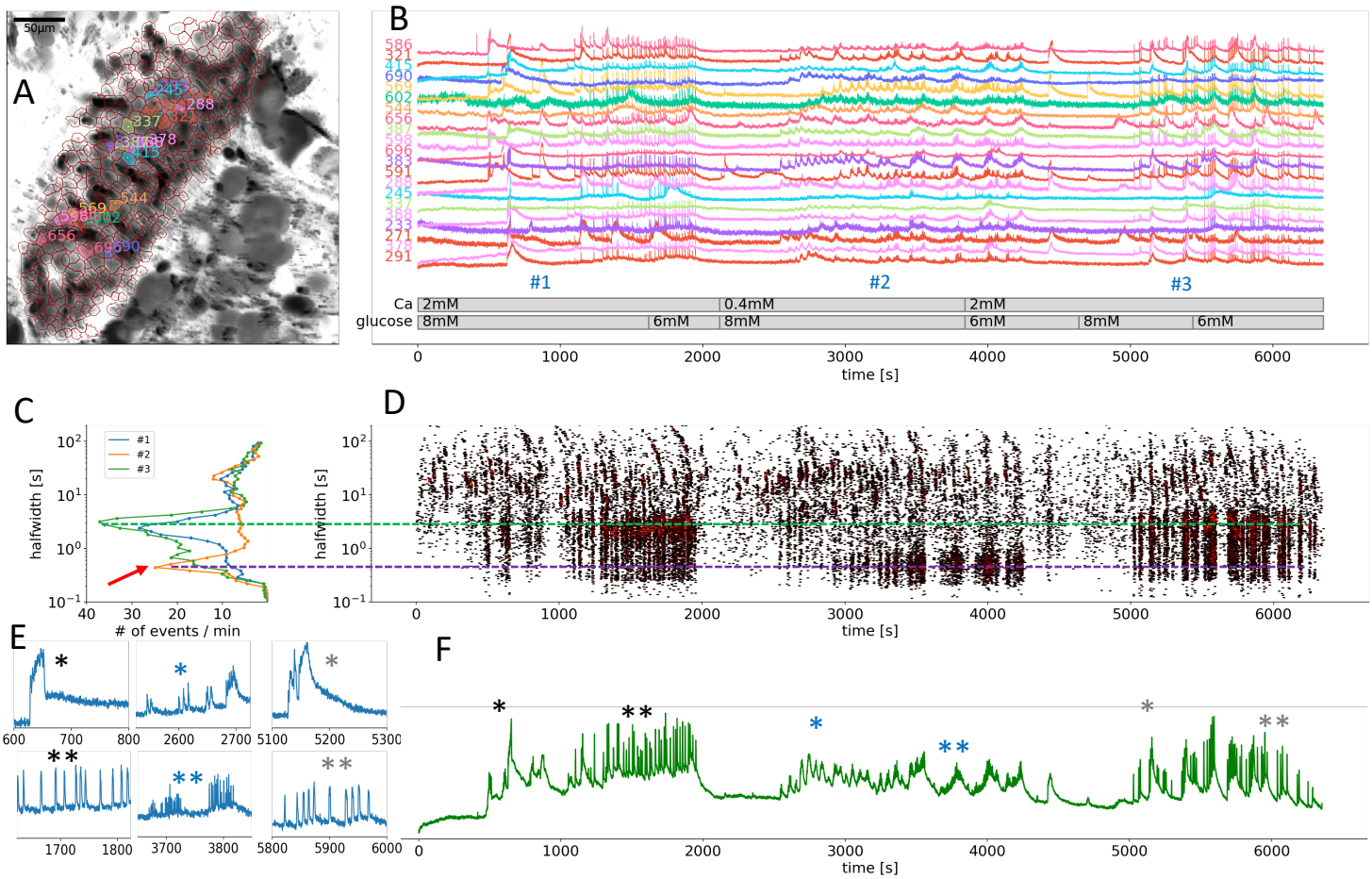

Figure 3. Glucose-dependent activation of beta cells at subphysiological extracellular Ca^{2+} concentration. **A**, Calbryte 520 staining of an islet in a fresh tissue slice. **B**, Time course of the $[Ca^{2+}]_c$ changes in a selection of beta cells indicated in the panel A, exposed to a triple 8 mM glucose stimulation protocol. Subphysiological extracellular Ca^{2+} level (400 μM) was applied in the middle section of the protocol. **C**, Frequency histograms of the event halfwidth durations and **D**, onset time of the $[Ca^{2+}]_c$ events at all measured time scales. Note the transient decomposition of fast events into high frequency shorter events, however, these short events were mostly still synchronized between the neighboring cells. **E**, Expanded time traces from a representative ROI indicating the a slow event from a transient phase (*) and a series of fast events during the plateau phase (**) as indicated in panel F. Asterisks from different sections of the protocol are color coded. **F**, Time trace of the average of all ROIs in the presented islet (n=374). There is a reduced superposition of the fast activity on the plateau phase in section 2.

2.3 $[Ca^{2+}]_c$ oscillations in low extracellular Ca^{2+} conditions

To isolate and test the potential role of intracellular Ca^{2+} channels on ER in the spatiotemporal regulation of $[Ca^{2+}]_c$ oscillations, we first used a classical approach with the reduction of extracellular $[Ca^{2+}]$ [53]. Incubation of beta cells with 0.4 mM extracellular Ca^{2+} uncovered two phenomena (Figure3). First, beta cells within the islets tended to functionally dissociate, losing coordinated and global intercellular Ca^{2+} oscillations with a phenotype resembling the Cx36 ablated or pharmacologically blocked cell-cell electrical coupling [52, 62]. Second, low extracellular Ca^{2+} also changed the pattern of $[Ca^{2+}]_c$ oscillations at all time scales (Figure 3EF). The most prominent effect of low extracellular Ca^{2+} was the complete absence of the dominant time scale

(Figure 3C), where the median halfwidth duration of 2.2 s (Q1 1.6 s, Q3 3.0 s) from the control sections 1 and 2.5 s (Q1 1.5 s, Q3 3.3 s) from the control section 3, shortened to 0.6 s (Q1 0.5 s, Q3 1.7 s, $p<10^{-200}$). The aforementioned fast $[Ca^{2+}]_c$ oscillations decomposed into series of higher frequency subsecond unitary events (Figure 3C-F), confirming previous observations [21]. The synchronization between the individual beta cells within the islet was more localized. All fast events could be recovered after reintroduction of normal extracellular Ca^{2+} concentration in the last phase of the experiment (Figure 3B,D). The slow oscillations were significantly longer in the low extracellular $[Ca^{2+}]$, with median halfwidth duration of 20 s (Q1 11 s, Q3 32 s) and 24 s (Q1 14 s, Q3 33 s, $p<0.0001$). These slow oscillations did not shorten after reintroduction of normal extracellular Ca^{2+} concentration and there median halfwidth duration was 24 s (Q1 13, Q3 43s, $p<0.0001$). Our results suggest that in the presence of sufficient extracellular Ca^{2+} concentration, the CICR-like $[Ca^{2+}]_c$ oscillations are likely to occur in glucose stimulated beta cells *in situ* and that these events decompose at unphysiologically low extracellular $[Ca^{2+}]$. The spectrum of recorded patterns of single beta cell activities confirms previously described role of CICR through intracellular Ca^{2+} channel in glucose-dependent activity of beta cells [33, 37].

2.4 Intracellular Ca^{2+} channels are sufficient to generate $[Ca^{2+}]_c$ oscillations at sub-stimulatory glucose

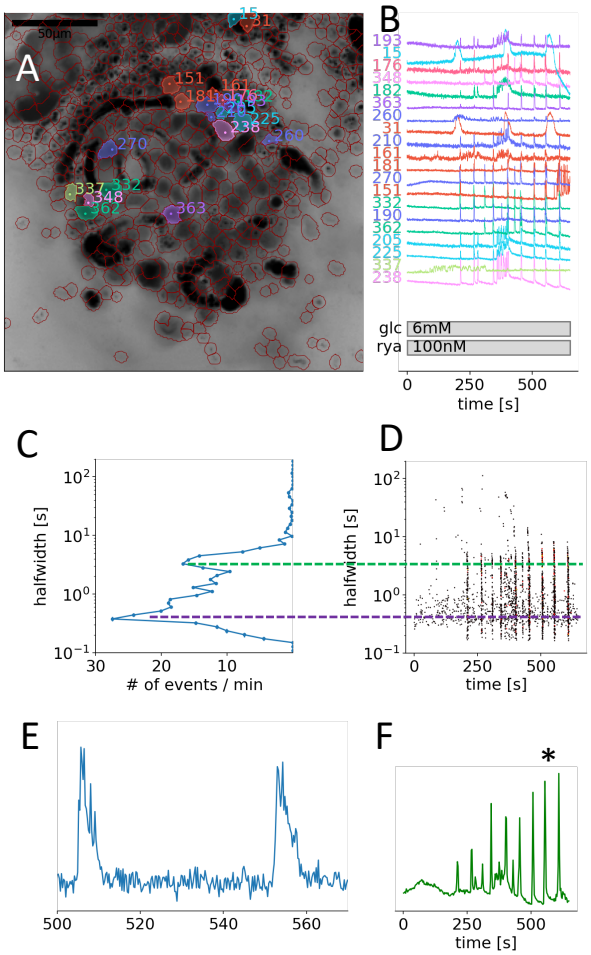

Figure 4. Pharmacological activation of intracellular RYR Ca^{2+} receptors in mouse beta cells at subthreshold glucose concentration. A, Calbryte 520 staining of a fresh tissue slice with labelled ROIs. **B**, Time course of the $[Ca^{2+}]_c$ changes in a selection of beta cells indicated in the panel A. The slice was exposed to 6 mM glucose and 100 nM ryanodine. Stimulatory ryanodine induced fast and synchronous $[Ca^{2+}]_c$ oscillations of the dominant time scale. Note two acinar cells responding to stimulatory raynodine with slower Ca^{2+} waves (ROIs 15,31). **C**, Frequency histograms of the event halfwidth durations and **D**, onset time of the $[Ca^{2+}]_c$ events at all measured time scales. Note the increased representation of a subsecond component forming the fast events. **E**, Expanded time of the two fast events from a representative ROI (*) as indicated in panel F. **F**,Time trace of the average of all ROIs in the presented islet (n=168). There is a prominent superposition of the fast activity on the plateau phases between the ROis.

Next, we directly assessed the role of RYR intracellular Ca^{2+} channels, which in beta-cells are predominantly RYR2 [74], in the glucose-dependent $[Ca^{2+}]_c$ oscillations. We first used methods of pharmacological RYR activation.

We showed that at subthreshold glucose (6 mM), direct stimulation with stimulatory concentrations of ryanodine (100 nM) elicited regenerative $[Ca^{2+}]_c$ oscillations (Figure 4B). The ryanodine-dependent fast $[Ca^{2+}]_c$ events were triggered. The dominant scale of $[Ca^{2+}]_c$ events after ryanodine stimulation was in the subsecond range, superimposed on top of the fast and coordinated fast events of the same duration as observed under control condition(Figure 4C-F). The onset of the activity varied significantly between the cells in an islet (Figure 4B).

The role of IP_3R was assessed indirectly using a saturating concentration of acetylcholine (ACh, 10 μM),

which activates muscarinic M_3 receptors and stimulates IP_3 production. At 6 mM glucose, 10 μM ACh initially produced a slow transient change, followed by a fast and regenerative $[Ca^{2+}]_c$ oscillations in a subset (up to 30 %) of beta cells (Figure 5). The fast oscillations during the plateau phase were not coordinated among beta cells in the active subset of cells in an islet and were typically the same duration compared to a dominant time scale in the glucose triggered response (Figure 5C).

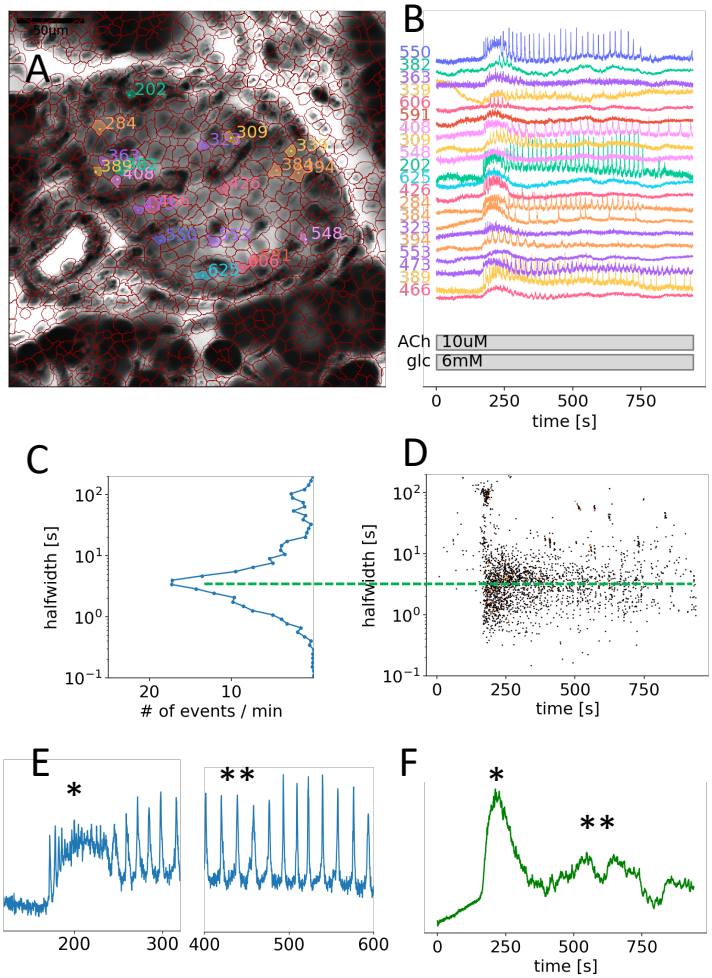

Figure 5. Pharmacological activation of intracellular IP_3 Ca^{2+} release channels in mouse beta cells at subthreshold glucose concentration. **A**, Calbryte 520 staining of a fresh tissue slice with labeller ROIs within the islet. **B**, Time course of the $[Ca^{2+}]_c$ changes in a selection of beta cells indicated in the panel A. The slice was exposed to 6 mM glucose and 10 μM ACh. ACh induced $[Ca^{2+}]_c$ oscillations in two phases. The first phase was dominated by large slow transients and partially synchronized Ca^{2+} oscillations among the cells. During the second phase, a regenerative faster activity was detected. **C**, Frequency histograms of the event halfwidth durations and **D**, onset time of the $[Ca^{2+}]_c$ events at all measured time scales. Note the predominantly asynchronous fast activity of the events in dominant time scale. **E**, Expanded time traces from a representative ROI indicating the a slow event from a transient phase (*) and a series of fast events during the plateau phase (**) as indicated in panel F. **F**, Time trace of the average of all ROIs in the presented islet (n=274).

Our results suggest that pharmacological activation of both RYR or IP_3 intracellular release channel could produce $[Ca^{2+}]_c$ oscillations in beta cells that would be typically observed during the 8 mM glucose stimulation. Both stimulations generated compound $[Ca^{2+}]_c$ events through inter-molecular CICR and present two distinct kinetic components for intracellular release of Ca^{2+} and distinct regimes of intercellular coordination. Together these data further confirm that a selective stimulation of Ca^{2+} release from the intracellular Ca^{2+} stores can independently drive $[Ca^{2+}]_c$ oscillations in beta cells that are both coordinated (Figure 4) or non-coordinated (Figure 5).

2.5 Intracellular Ca^{2+} channels are necessary for glucose-induced $[Ca^{2+}]_c$ oscillations

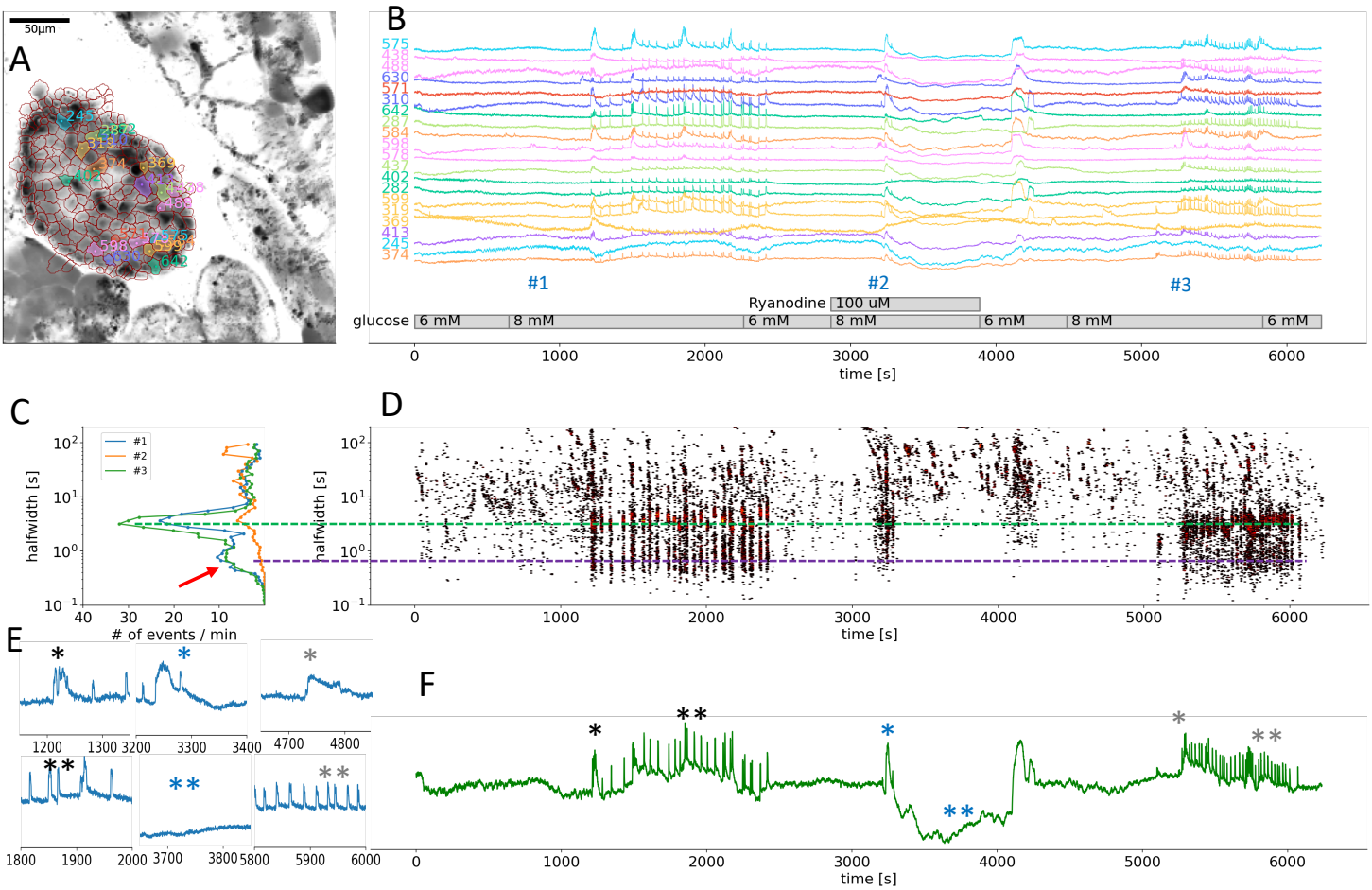

Figure 6. Pharmacological inhibition of intracellular RYR Ca^{2+} channels in mouse beta selectively inhibits the plateau $[Ca^{2+}]_c$ oscillations . **A**, Calbryte 520 staining of a fresh tissue slice with labelled ROIs within the islet. **B**, Time course of the $[Ca^{2+}]_c$ changes in a selection of beta cells indicated in the panel A, exposed to a triple 8 mM glucose stimulation protocol. Inhibitory ryanodine (100 μM) was applied in the middle section of the protocol. **C**, Frequency histograms of the event halfwidth durations and **D**, onset time of the $[Ca^{2+}]_c$ events at all measured time scales. Note the complete absence of the events of the dominant time scale and reduced $[Ca^{2+}]_c$ during the exposure to high ryanodine. **E**,. Expanded time traces from a representative ROI indicating the a slow event from a transient phase (*) and a series or an absence of a seies of fast events during the plateau phase (**) as indicated in panel F. Asterisks from different sections of the protocol are color coded. **F**, Time trace of the average of all ROIs in the presented islet (n=219).

After demonstrating that $[Ca^{2+}]_c$ oscillations can be evoked at glucose concentrations just below the glucose activation threshold with both RYR and IP_3 receptor activation, we used specific pharmacological tools to selectively block the activity of these intracellular channels and to determine the contribution of these receptors to the glucose-dependent stimulation of $[Ca^{2+}]_c$ oscillations. We blocked RYR intracellular Ca^{2+} channels with an inhibitory ryanodine concentration (100 μM)(Figure 6). High ryanodine selectively and completely inhibited the dominant time scale of oscillations and its superimposed subsecond events during the plateau phase, leaving

initial slower transient changes intact (Figure 6C). Immediately after the washout of the high ryanodine, we observed prominent slow $[Ca^{2+}]_c$ oscillations (Figure 6B-D).

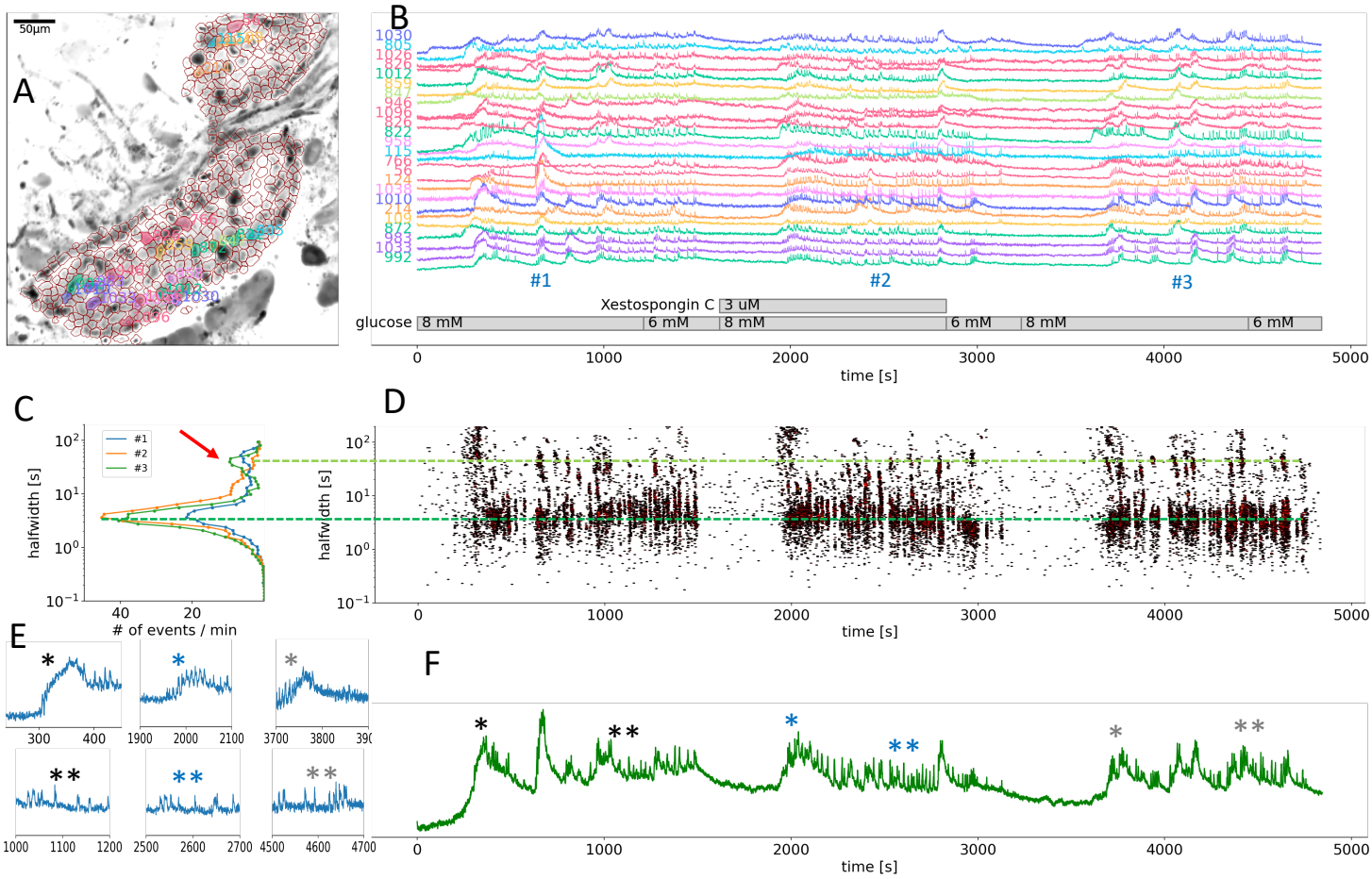

Figure 7. Pharmacological inhibition of intracellular IP_3 Ca^{2+} channels in mouse beta cells selectively inhibits the slow $[Ca^{2+}]_c$ oscillations during the transient phase. **A**, Calbryte 520 staining of a fresh tissue slice with labelled ROIs within two neigboring islets. **B**, Time course of the $[Ca^{2+}]_c$ changes in a selection of beta cells indicated in the panel A, exposed to a triple 8 mM glucose stimulation protocol. Xestospongine C (3 μM), a selective IP_3 receptor inhibitor, was applied in the section 2 of the protocol. **C**, Frequency histograms of the event halfwidth durations and **D**, onset time of the $[Ca^{2+}]_c$ events at all measured time scales. Note the transiently reduced frequency of the slow events with a duration of several tens of seconds during the exposure to Xest C (light green dashed line). **E**, Expanded time traces from a representative ROI indicating the a slow event from a transient phase (*) and a series of fast events during the plateau phase (**) as indicated in panel F. Asterisks from different sections of the protocol are color coded. **F**, Time trace of the average of all ROIs in the presented islet (n=445, two islets).

We also blocked the activity of IP_3 intracellular Ca^{2+} channels using 3 μM Xestospongin C. This specific inhibitor of IP_3 channels selectively and to a significant extent blocked the $[Ca^{2+}]_c$ events during the initial transient and asynchronous pathway, while the plateau phase fast oscillations remained unaffected (Figure 7). The Xestospongin C manipulation was reversible after a 6 mM glucose washout period and a repeated stimulation with 8 mM glucose (Figure 7B-D).

These data provide additional evidence regarding the existence of two distinct kinetic components for the activation and activity of beta cells. The initial kinetic

component during the activation of beta cells in the fresh pancreas slice consisted of one or few IP_3-dependent $[Ca^{2+}]_c$ transients (some tens of seconds long), followed by a sustained component comprising a series of faster RYR-mediated events (several seconds long). This pattern repeated itself during the repetitive bursts during 8 mM glucose stimulation (Figure 1).

3 Discussion

In the current study, we combined fast confocal microscopy, a photostable and bright low affinity Ca^{2+} sensor, and tools of data sciences to obtain new insights into physiological activation of beta cells within intact islets in fresh pancreas tissue slices. Based on the unique spatiotemporal resolution of our approach and our data with specific modulation of Ca^{2+} release channels, we propose an updated model of beta-cell activation and bursting activity in the physiological glucose range that would be observed after a meal (Figure 8). According to our model, multiple forms of oscillatory activity are generated with temporal superposition of two basic processes: (i) oscillations in the time domain from a few seconds to tens of seconds, which represent CICR of either IP_3 or RYR Ca^{2+} release channels, which can be both directly influenced by glucose metabolism, and (ii) oscillations in a sub second time domain which represents unitary activity of the same channels. For our model and as described in other cell types, CICR events are dependent on sufficient Ca^{2+} ER load [12, 26].

CICR in beta cells involving both IP_3 and RYR2 release channels has been previously reported [16, 17, 35]. When, however, the ER Ca^{2+} load decreases, CICR bursts switch to subsecond events produced by individual or more localised clusters of intracellular Ca^{2+} release channels before oscillations eventually stop. Decomposed CICR bursts therefore appear to oscillate at higher frequency, a phenomenon reported after ER emptying using thapsigargin [73], genetic ablation of L-type VACCs [58], or lowered extracellular Ca^{2+} [21, 73]. Our experiments show that physiological glucose concentrations (e.g. 8 mM) support sufficient ER Ca^{2+} load [69] to enable CICR bursts triggered by direct pharmacological stimulation of RYR and IP_3 Ca^{2+} channels. Addition of suprathreshold glucose concentration first activates a prominent, Xestospongin C-sensitive IP_3-dependent transient Ca^{2+} release lasting for several tens of seconds. IP_3 activation is localized to segregated beta cells clusters and not coordinated within the whole islet [44]. Next, Ca^{2+} -dependent mitochondrial metabolism of glucose boosts ATP production [57], that directly decreases the opening probability of K_{ATP} channels [64], and directly activates RYR Ca^{2+} release channels [34, 71]. High input resistance due to K_{ATP} channel closure enhances the coordination between beta cells during the regenerative RYR-CICR activity. However, we also observed synchronized activity after ryanodine stimulation at substimulatory glucose and coordinated activity was specifically eliminated by inhibitory concentrations of ryanodine, suggesting that RYR independently promotes intercellular coordination due to strategic cellular localization of these receptors (Figure 9). The long-term RYR activity and occasional slow IP_3 Ca^{2+} transients during the plateau phase of beta cell activity must be supported with mobilization of Ca^{2+} from the extracellular compartment, where VACCs activate trough a large ER Ca^{2+} depletion [73].

Our results do not discount a role for plasma membrane K_{ATP} channels and voltage gated Ca^{2+} entry in beta cell function. In our updated model, K_{ATP} channels play a critical depolarizing role to support activation of L-type VACCs, reloading of ER Ca^{2+} stores, cell-cell coordination and the long-term regenerative activity, consistent with the human genetics of beta-cell responsiveness and their clinical utility as targets of sulphonylurea therapy [50]. K_{ATP} channels may also play an outsized role in the response to an instantaneous glucose increase from hypoglycemic levels (2-3 mM) to

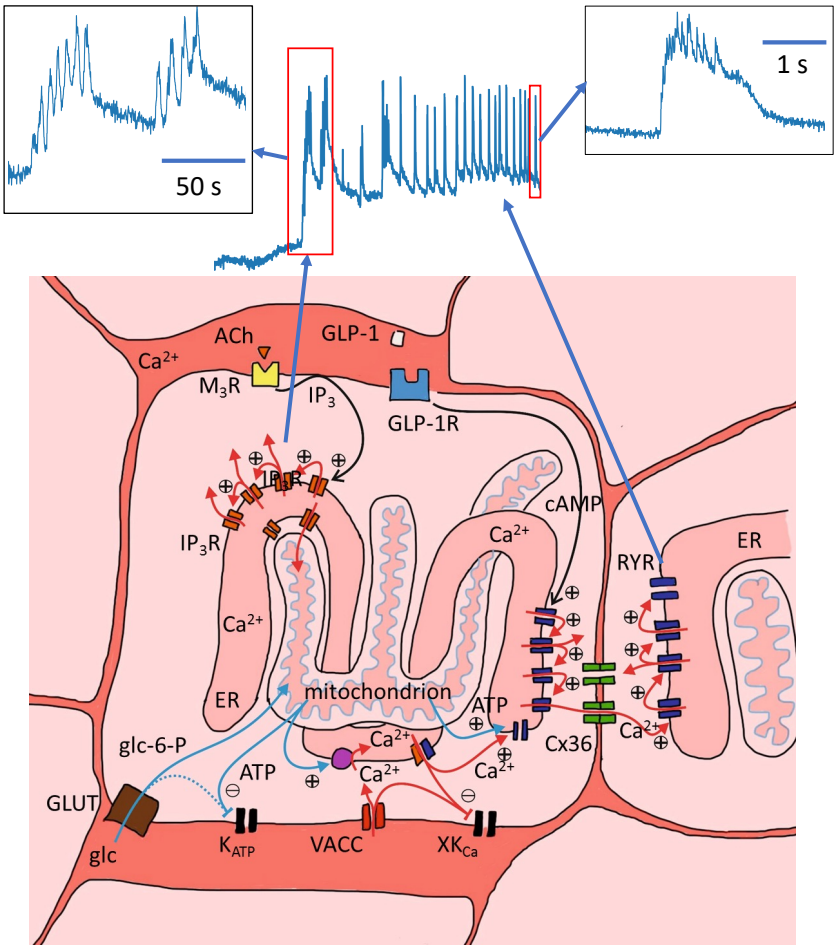

Figure 8. Proposed model of the role of intracellular RYR and IP_3 Ca^{2+} release channels in activation and activity of the mouse beta cell. The basic principle in different patterns of $[Ca^{2+}]_c$ oscillation is CICR. In the process of physiological glucose stimulation, a tonic ACh stimulation and lower Ca^{2+} threshold for activation, initially produces one or two slow waves of IP_3Rs´ activity (inset top left), which is followed by repetitive CICR bursts of RYRs´ activity (inset top right), both together producing a typical biphasic response. The arrangement of RYR receptors enables intercellular communication through the Cx36 proteins and synchronized propagation of the Ca^{2+} events. ATP-dependent closure of K_{ATP} channels contributes to the synchronization. VACCs are critical for refilling of the internal stores. $[Ca^{2+}]_c$ changes are registered by different Ca^{2+}-dependent K^+ channels (XK_{Ca}). GLP-1R stimulation and ATP from the glucose metabolism can also modulate the RYR activity. $[Ca^{2+}]$ in the extracellular space and in different compartments of the cell is color coded, with the lowest $[Ca^{2+}]$ in the cytosol.

super-physiological levels (15-25 mM), but we demonstrate here that glucose-dependent activation of K_{ATP} channels is not required for activation of beta cells at 8 mM glucose, consistent with previous observations suggesting closure of K_{ATP} channels is not the sole mechanism to depolarize beta cells [3]. Indeed, other plasma membrane ionic currents have been invoked to explain the complex oscillatory behaviour of beta-cells [4, 54]. As an example, multiple Ca^{2+}-dependent K^+ and other K^+ channel activities have been bundled to explain the elusive, so called K_{slow} conductance, that should critically shape the typical bursting pattern of beta cells after initial beta cell activation [1, 2, 24, 68]. Additional validation is required in human islets to define the role of these modulatory plasma membrane ion channels in physiological glucose responses [31].

Glucose plays an essential role in filling, and therefore also emptying, intracellular Ca^{2+} stores [69]. Forced depletion of intracellular Ca^{2+} stores using thapsigargin or extracellular EGTA increases cytosolic Ca^{2+} concentration and produces sustained depolarization, with increased frequency of membrane potential oscillations [73]. Similarly, reduced activity of the SERCA2 pump to maintain ER Ca^{2+} loading disrupts glucose-stimulated calcium signaling [70]. Increased frequency of $[Ca^{2+}]_c$ oscillations was also recorded in our experiment using low extracellular Ca^{2+} concentration. We demonstrate that glucose around the threshold (6-7 mM glucose) supports ER Ca^{2+} release through IP_3 and RYR release channels. In addition to supporting sufficient Ca^{2+} load in the ER, glucose-dependent effects in beta cells provide all key substrates, like ATP and cAMP, to directly trigger and modulate the activation of intracellular Ca^{2+} release channels, even in the absence of changes in membrane potential. Included in these stimuli is the parasympathetic release of ACh binding to muscarinic ACh receptors (mAChRs) and induce insulin release via the production of IP_3 and Ca^{2+} release from the intracellular stores [10, 14, 22, 61]. The role of RYR and IP_3 receptors has likely been systematically underestimated, including in our own previous studies, due to pre-emptying of intracellular Ca^{2+} stores in previous studies that were initiated at 2-3 mM glucose.

The prominent role for intracellular Ca^{2+} release had strong early support from $^{45}Ca^{2+}$ flux studies [72], but subsequent electrophysiological work challenged this paradigm [34, 73] and evidence accumulated in favor of the dominance of plasma membrane K^+ channels and VACCs in patterning $[Ca^{2+}]_c$ oscillations. Even the presence of RYR Ca^{2+} channels in beta cells was debated [5, 51], although there is less controversy regarding the expression and roles of IP_3Rs [13, 28]. However, we and others have documented RYR activity and confirmed RYR2 as the most abundant isoform expressed in rat, mouse, and human beta cells [36, 42, 67, 74]. Indeed, the unique localization and Ca^{2+}-release kinetics of each intracellular Ca^{2+} release channel enables the coding of Ca^{2+} signals to control specific cellular functions [6–8, 36].

It has been proposed that the beta cell ER is extraordinarily leaky to Ca^{2+} [38]. ER Ca^{2+} leak is accelerated by ER stress, leading to beta cell apoptosis [42, 74]. Also excitotoxicity and ER Ca^{2+} overload have been implicated in beta cell apoptosis [74] and may also contribute to diabetes pathogenesis. There is strong evidence that ER dysfunction is involved in the pathogenesis of both type 1 and type 2 diabetes [19]. In type 1 diabetes, ER dysfunction is a prominent and early feature [41]. In type 2 diabetes, GWAS has identified multiple RYR2 SNPs with suggestive evidence in dozens of glycemic traits (www.type2diabetesgenetics.org, accessed Feb 2021) [60].

Both ER Ca^{2+} load as well as intracellular Ca^{2+} channels can serve as targets for therapy of diabetes mellitus [30]. Pharmacological inhibition of VACCs activity with verapamil was recently reported to have a positive effect on beta cell function and survival in adults with recently diagnosed T1D [49], consistent with previous pre-clinical studies [11]. Pre-clinical studies also demonstrate that inhibition of voltage-gated Na^+ channels can protect beta cells, and NOD mice from diabetes [40, 75]. Also, intracellular

Ca^{2+} release channels are druggable and have been implicated in successful diabetes therapies. For example, RYR2 receptors can be activated by both ATP and PKA [71] and can therefore be directly stimulated by glucose and modulated by incretins. RYR are a proposed therapeutic target in Wolfram syndrome [18]. Abundant physiological data also indicate that CICR from intracellular stores can serve as an "amplifier" of glucose-induced insulin granule exocytosis and plays a central role in incretin-induced insulin secretion [9, 37].

In summary, using powerful new rapid imaging and data analysis methods, we show here that IP_3R and RYR play essential roles in glucose stimulated Ca^{2+} signaling in beta cells *in situ*. We define roles for glucose and plasma membrane Ca^{2+} influx ER Ca^{2+} store refilling and sustained oscillatory activity. We provide an updated model of physiological glucose signaling.

4 Materials and Methods

4.1 Ethics statement

We conducted the study in strict accordance with all national and European recommendations on care and handling experimental animals, and all efforts were made to minimize the suffering of animals. The Ministry of Education, Science and Research, Republic of Austria (No: 2020-0.488.800) and administration of the Republic of Slovenia for Food Safety, Veterinary and Plant Protection (No: U34401-12/2015/3) approved the experimental protocol (No: U34401-12/2015/3).

4.2 Tissue slice preparation and dye loading

C57BL/6J mice, 8–20 weeks of age, and of either sex (Jackson Laboratories), were kept on a 12:12 hours light: dark schedule in individually ventilated cages (Allentown LLC, USA) and used to prepare pancreatic tissue slices, as described previously [63, 65]. In brief, after sacrificing the mice, we accessed the abdominal cavity via laparotomy and distally clamped the common bile duct at the major duodenal papilla. Proximally, we injected the low-melting-point 1.9 % agarose (Lonza, USA) dissolved in extracellular solution (ECS, consisting of (in mM) 125 NaCl, 10 HEPES, 10 $NaHCO_3$, 6 glucose, 6 lactic acid, 3 myo-inositol, 2.5 KCl, 2 Na-pyruvate, 2 $CaCl_2$, 1.25 NaH_2PO_4, 1 $MgCl_2$, 0.25 ascorbic acid) at 40 °C into the common bile duct. Immediately after injection, we cooled the agarose infused pancreas with ice-cold ECS and extracted it. We prepared tissue slices with a thickness of 140 µm with a vibratome (VT 1000 S, Leica) and collected them in HEPES-buffered saline at RT (HBS, consisting of (in mM) 150 NaCl, 10 HEPES, 6 glucose, 5 KCl, 2 $CaCl_2$, 1 $MgCl_2$; titrated to pH=7.4 using 1 M NaOH). For staining, we incubated the slices for 50 minutes at RT in the dye-loading solution (6 µM Calbryte 520, AAT Bioquest), 0.03 % Pluronic F-127 (w/v), and 0.12 % dimethylsulphoxide (v/v) dissolved in HBS). The Ca^{2+} fluorescent dyes from a Calbryte series are highly fluorescent and photostable, allowing long-term recording even in deeper layers of the tissue slice. The linear part of the Ca^{2+}-binding curve for Calbryte 520 (K_D of 1.2 μM) captures the $[Ca^{2+}]_c$ changes in beta cells better than the high affinity sensors we routinely used in our imaging experiments before. All chemicals were obtained from Sigma-Aldrich (St. Louis, Missouri, USA) unless otherwise specified.

4.3 Stimulation protocol and cytosolic calcium imaging

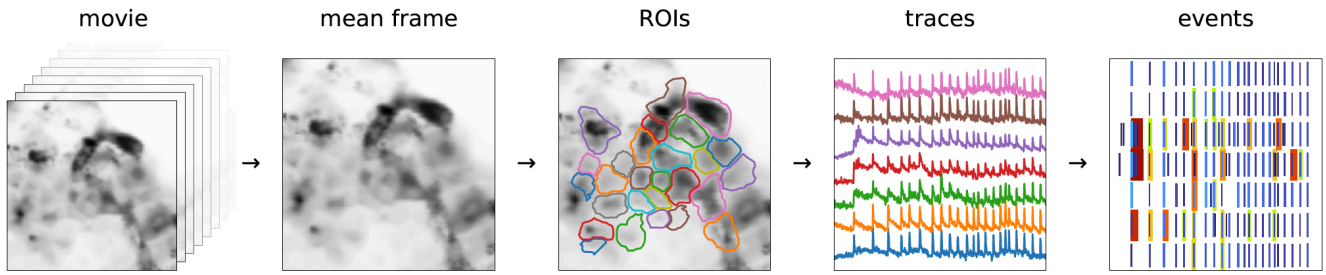

Figure 9.Processing pipeline to automatically detect ROI and $[Ca^{2+}]_c$ events at all time scales within an experiment. From a full movie, we calculated the mean (or other statistic) across all frames. We passed the mean image through a band-pass filter and define ROIs by detecting local peaks of light intensity. We then saved ROIs with all the important information (time traces, ROI coordinates, movie statistics, recording frequency, pixel size, etc.). Traces contained features at very different timescales - with different timescales presumably being important for different cell types. We collected them into separable events for analysis.

We transferred individual pancreatic slices to a perifusion system containing 6 mM glucose in HEPES-buffered ECS at 34 °C. At least 3 slices/mice were used for each experimental condition. Slices, with the exception of experiments presented in Figs. 4 and 5, were exposed to a series of three square-pulse-like stimulations (triple protocol) characterized by exposure to 8 mM glucose for 25 minutes, followed by a washout with sub-stimulatory 6 mM glucose concentration until all the activity switched off. We typically applied the pharmacological treatment during the second section of the triple protocol. Imaging was performed on standard confocal microscopes equipped with resonant scanners (Leica Microsystems TCS SP5 and SP8 or Nikon A1R) both upright and inverted with their respective sets of 20x high NA objective lenses. Acquisition frequency was set to at least 20 Hz at 256 x 256 pixels, with pixels size close to 1 μm^2 to allow for a precise quantification of $[Ca^{2+}]_c$ oscillations. Calbryte 520 was excited by a 488 nm argon laser (Leica SP5 and Nikon A1R) or 490 nm line of a white laser (Leica SP8). The emitted fluorescence was detected by HyD hybrid detector in the range of 500-700 nm using a photon counting mode (Leica) or GaAsP PMT detectors (Nikon).

4.4 Analysis and processing of data

The general analysis pipeline was as follows. Experiments involving imaging of pancreatic slices typically focused on a single field of view showing up to hundreds of cells, in a recording of at least several, often dozens, gigabytes. Current tools that are widely used (e.g., ImageJ) rely on loading the recording, or its part, into memory, for viewing, analysis, and processing. It also requires laborious and long human engagement. We have developed a set of interdependent tools to automatize as much as possible the analysis pipeline (Figure 9, Supporting information).

Semi-automatic detection of regions of interest was identified as follows. Recordings were stored as a 3-dimensional ($T \times X \times Y$) numpy array [29]. When the recording was stable, obtaining a mean image, or any other statistic over frame, was rather trivial. In case there was horizontal movement, it could be corrected for by aligning the frames to a template. For this we used the functionality present in CaImAn [23], except that high frequency recordings needed to be rebinned to some moderate frequency (a few Hz), before correcting, in order to reduce the noise level. Once the translation offsets were

obtained, we used them to correct the recording in original frequency. To define regions of interest, we blurred the representative image by a kernel of the size we expect cells to be, and at the scale double of that. The difference between these two images represents a band-pass filter of the original, where the local intensity variations were emphasized (Figure S9-1). We then passed through all pixels where the value of the filtered image was positive (or larger than a small positive threshold), and for each pixel we searched for a local peak in its vicinity. All the pixels that lead to the same local peak were then grouped into a single ROI. As we were mainly interested in islet cells, we chose the kernel size to approximately correspond to 10 μm, which is the characteristic length scale of the islet cells. If the pixel size is unknown, the choice of kernel is up to the person running the scripts.

Representative image can be a mean over all frames or any other statistic. In addition, our code supports standard deviation, mean and standard deviation of the first derivative of the movie, and a "robust maximum" of the movie. As "robust maximum", we defined a very high percentile of the set absolute values of a set, essentially a value close to its maximum, by default it is 10th largest. We avoid the maximum as a means to make analysis robust to outliers. This statistic is sensitive to cells which fire extremely rarely during a recording, so that the mean of those pixels is negligible. By default, we choose an average of the mean and high percentile as a representative image for band-pass filtering and ROI extraction.

Trace processing was conducted as follows. In an ideal detector, recording a time trace of a single pixel in absence of any signal would consist of independent values of the number of photons detected during the dwell time. The values (x) are then distributed according to the Poisson distribution, with standard deviation (σ_1) being equal to the square root of the mean μ_1, $\sigma_1 = \sqrt{\mu_1}$. Tranformation to standard score or z-score (Figure S9-2) with $z = \frac{x-\mu}{\sigma}$ is then performed that recasts the initial quantity x in the units of standard deviation from the expected mean. A noisy trace in z spends 95% of the time between -2 and 2, and 99.7% between -3 and 3. Probability of $z > 3$ is very small $p < 0.0013$, which is why it is often considered a threshold value for pointing out the outliers. In general, the mean slow component needed to be inferred, typically by low-pass filtering. Throughout this project, we used cascaded second-order section (sos) filtering, implemented in `scipy.signal` module [23]. The cut-off frequency f_{cut} of a filter determines the timescale of the events that can be detected in z-score.

Fast Fourier transform naturally distorts signals, but the inferred z-score can be used to correct for it. We constructed an iterative filtering algorithm, where at each iteration, we neglect the outlier values of the original trace, substitute them with the values of the slow component, and reapply the filter. At each iteration, the distortion is less prominent, increasing the z-score. In Fig. S9-2, we show the result after 10 iterations, though we found three iterations as a more conservative choice, and a reasonable compromise between results and computing time.

All above refers also to a sum of pixel traces, but, crucially, not to their mean. A sum of two pixels a and b ($x = x_a + x_b$), with means μ_a and μ_b, would have a standard deviation as expected $\sigma = \sqrt{\mu} = \sqrt{\mu_a + \mu_b}$. But, if we were to consider the average $\tilde{x} = x/2$, standard deviation would be $\sqrt{2}$ times smaller $\tilde{\sigma} = \sigma/\sqrt{2}$. Therefore, when calculating z-score for a ROI trace, we always considered the sum, rather than the average trace of the underlying pixels. When we visualized traces, we show them averaged, only to keep the scales comparable. The same reasoning holds for rebinning a single trace, where the resulting trace, rebinned by a factor of n, had a standard deviation $\sqrt{n}$ times smaller than the original.

Experiments discussed in this manuscript were recorded on standard Leica SP5 or SP8, as well as NIKON A1R confocal microscopes. In cases where we used a Hybrid detector in the photon counting mode (Leica) we saw no significant departure from our

assumption of Poisson distribution. Even with non-unit gain, the linear dependence between variance and mean remains, though the slope was different from 1 (Figure S9-3). Other types of detectors introduce additional sources of noise other than Poisson (eg. thermal), but mostly they were still dominated by Poisson in our experience, at least as long as the values between neighboring pixels and frames were independent.

Traces contain features spanning orders of magnitude in time: from tens of milliseconds, to tens of minutes. We aimed to investigate how these events at different timescales and a connection between them and the islets' environment interact. For this, we devised a two-step algorithm to identify intrinsic timescale of events and to minimize false positives (Figure S9-4). In the first step, we performed a sequential filtering of the traces at timescales starting from 0.5s, and increasing by a factor of $\sqrt[4]{2}$, $\tau = \{2^{-1}, 2^{-3/4}, 2^{-1/2}, 2^{-1/4}, \ldots\}$, until the timescale of the longest event of interest was achieved. At each timescale, we transformed the trace to z-score, and identify regions where $z > 4$ as *candidate events*.

Events were characterized by the start time ((t_0), its maximal height, and the width at the half of the height (*halfwidth*, δt), which is our measurement of its duration. For simplicity, we defined end time as $t_{\text{end}} = t_0 + \delta t$, although events arguably last much longer after the intensity drops at half of the peak.

For an event to be considered real, it needed to be detected at multiple timescales, and will have started around the same time and will have approximately the same halfwidth. We specify a tolerance of 20 % of the halfwidth as to whether two candidate events should be considered equal; if their start and end times were within 20 % of the halfwidth, they were considered cognates, having arisen due to the same real event. For a set of cognates, we estimated the start and end time of the real underlying event as a median over the set. If the resulting estimate for the halfwidth is larger than 2 s, we required that a set consists of at least 4 candidate events (corresponding to event being detectable when filtered at timescales that differ at least two-fold). For shorter events, we required only that an event is not unique to a single timescale.

We also neglected events that last less than 3 time-frames, as well as those too close to the beginning or end of the recording (within $\delta t/2$), which we ascribed to artefacts from zero-padding for the filtering. We termed this procedure event *distilling* (Figs. 9, S9-4).

Supporting Information

S1 Figure

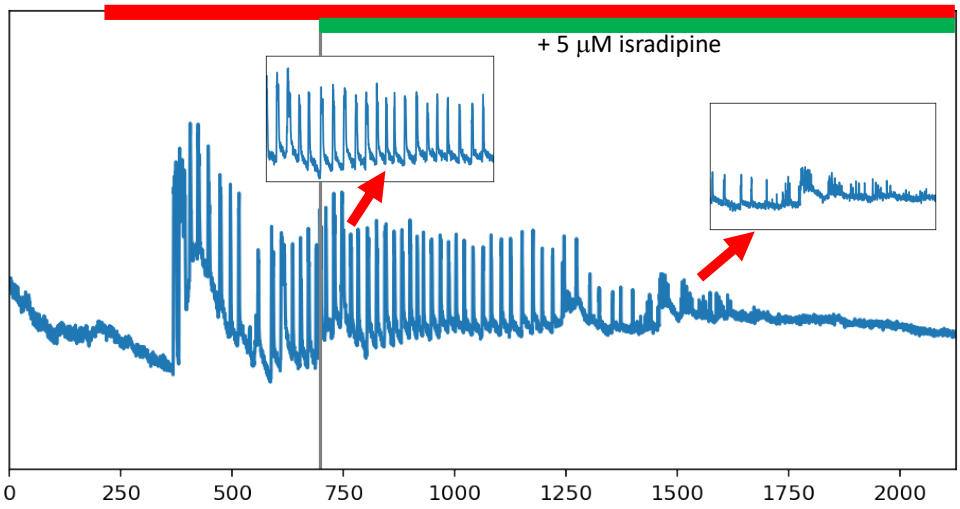

Figure S2-1. Delayed blockage of the glucose-dependent activity with isradipine. Time profile of the representative cell stimulated with 8 mM glucose (top red bar) and treated with isradipine during the plateau phase (green bar). Insets indicated by the red arrows show the change in the shape and frequency of the oscillations, with shortened duration and eventual complete stop of the activity.

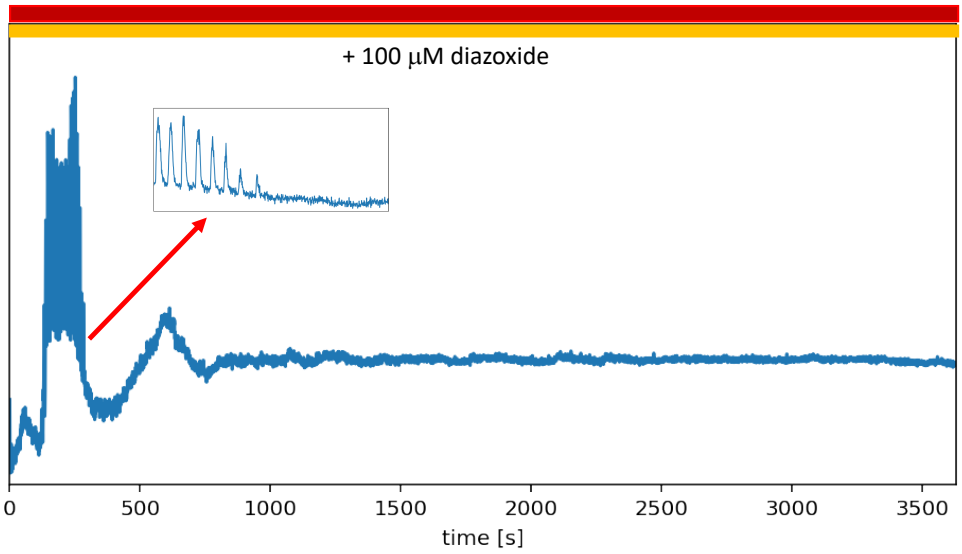

Figure S2-2. Activation of beta cells with hyperpolarized membrane potential. Time profile of the representative cell stimulated with 16 mM glucose (dark red bar) exposed to high concentration of the K_{ATP} channels opener (diazoxide, orange bar). At this high glucose concentration, all beta cells activate within a short time period, but persist only for a few minutes due to the presence of diazoxide. Inset indicated by the red arrow shows the change in the shape of the oscillations, with shortened duration and eventual complete stop of the activity.

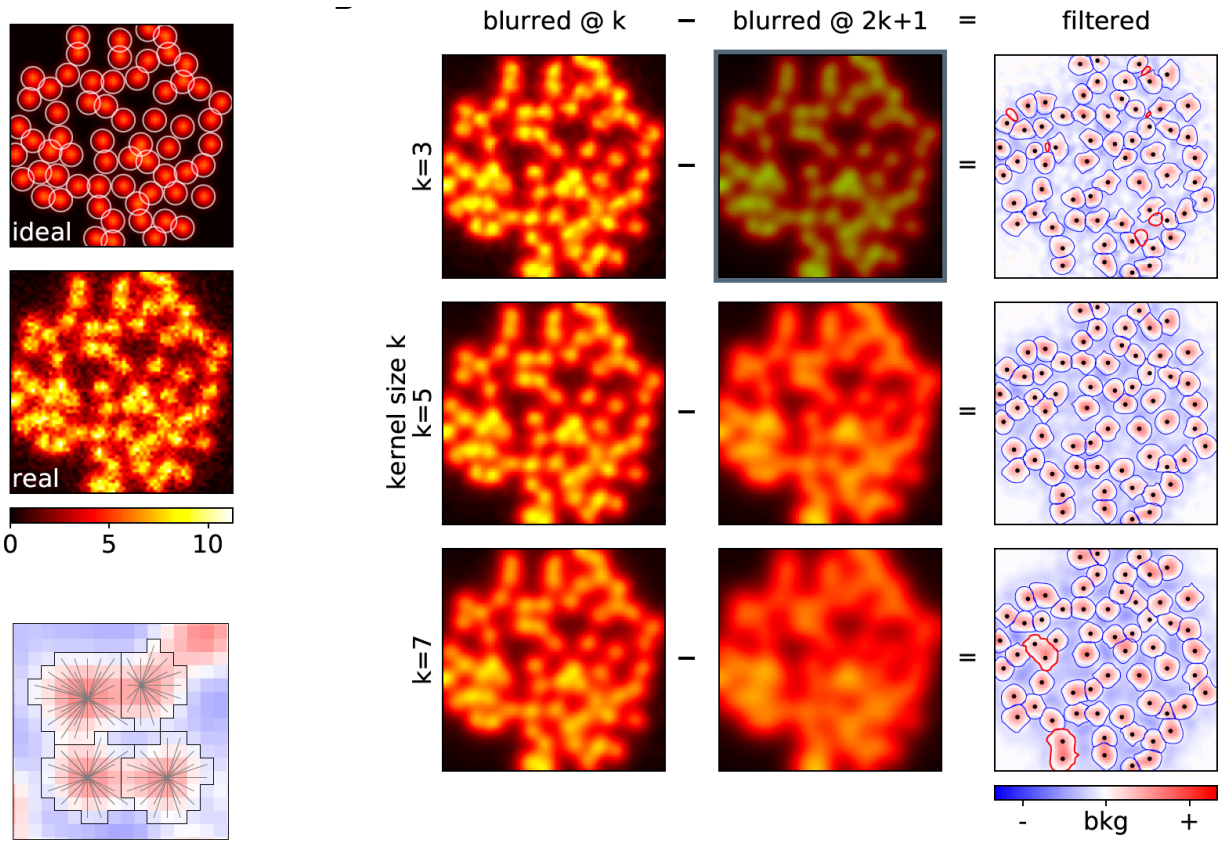

Figure S9-1. A, Computationally created template 64×64 image with uniform spherical cells, and with Poisson noise added.**B**, Band-pass filtering of the "realistic" image from A, with different kernel sizes, for denoising (*left*), and for approximating background (*middle*). The difference is the filtered image, used to construct ROIs (*right*). The size of the kernel determines the approximate size of the ROIs obtained. In thick red contours we emphasize misidentified ROIs; the dots indicate the real locations of the cells' centers. **C**, Each ROI is constructed by explicitly searching for a closest peak in intensity. A pixel can only be part of a single ROI.

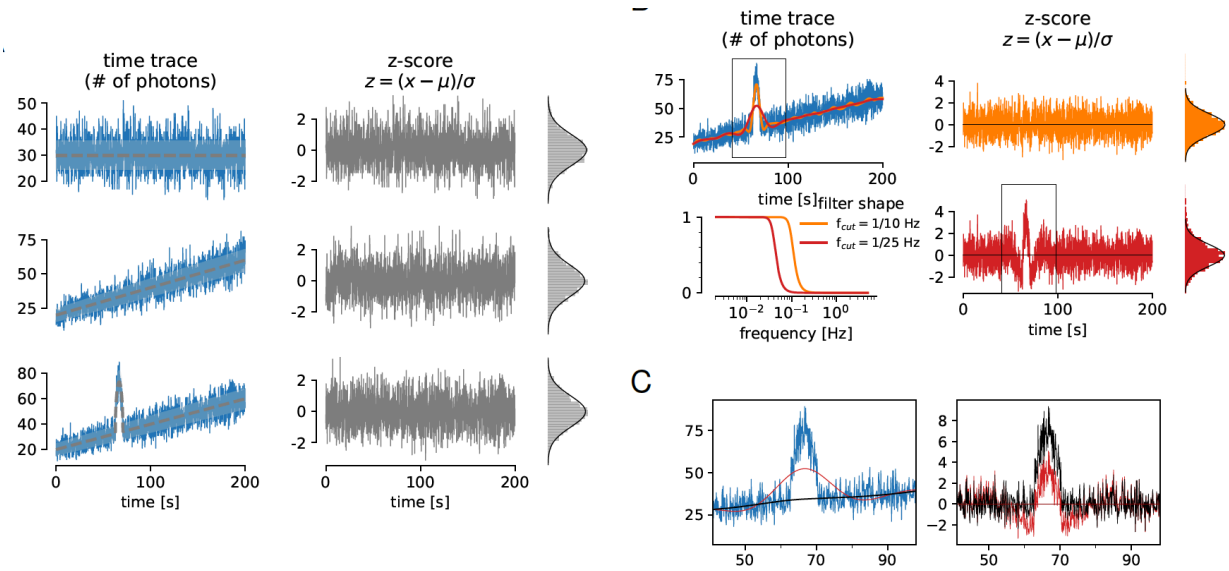

Figure S9-2. A, *Left*: Simulated traces with Poisson noise (blue) around different means (grey) with different temporal features. The shaded area represents one standard deviation interval around mean. *Right*: Irrespective of the shape of the mean, z-score transformation behaves exactly as a Gaussian variable with zero mean and unit standard deviation. **B**, The values of z-scores depend on the reference. In subfigure (A), the reference curves are known, but in general they need to be inferred, typically by low-pass filtering. The cut-off frequency f_{cut} of a filter determines the timescale of the events that can be detected in z-score. If filtered with too high cut-off (orange), the resulting smooth curve follows too closely the trace and the event is not visible in z. With $f_{cut} = 1/50$ Hz, the resulting z-score has obvious outliers ($z \geq 3$), visible both in trace and in the histogram. **C**, Zoom to the indicated regions form B. The original (blue) and the filtered trace and z-score (red), and the filtered trace and z-score corrected for distortion (black).

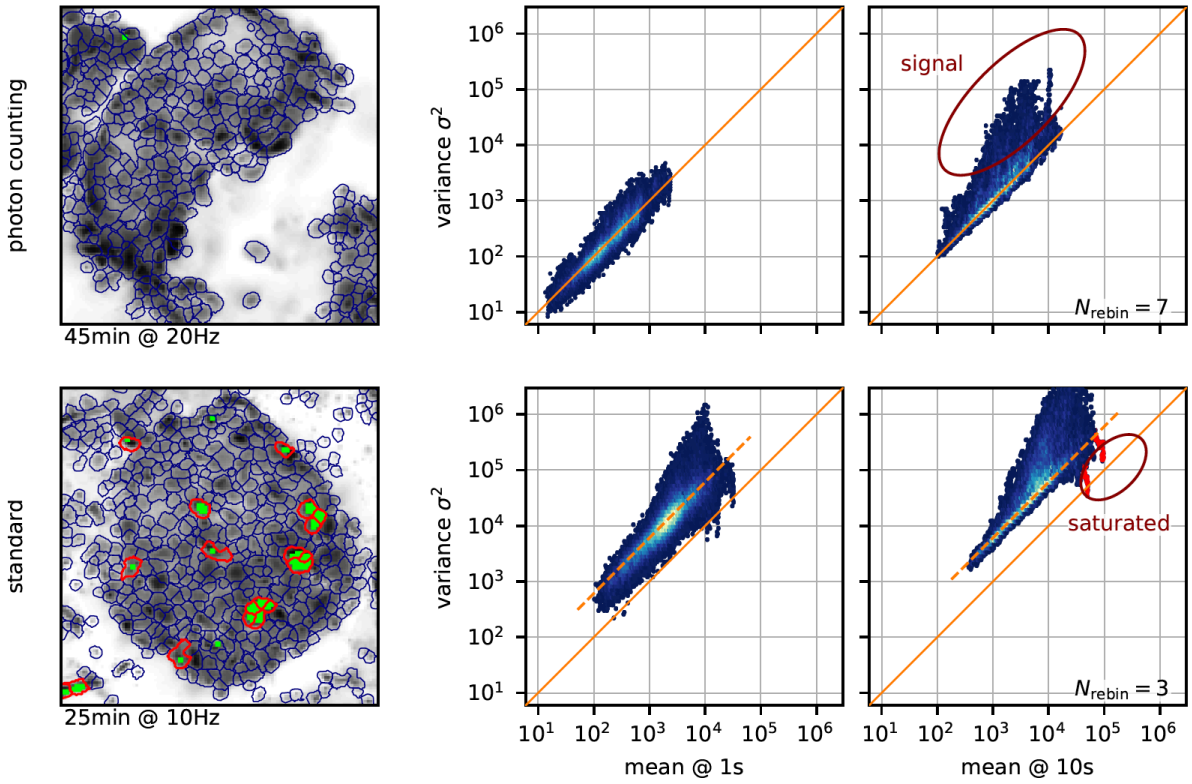

Figure S9-3. A, *Left*: Regions of interest for the two experiments recorded using the raw photon-counting mode (*top*, used for **Fig.1** in the main text), and the standard mode with large gain (*bottom*). Pixels which had at least 10 saturated values are shown in green. In thick red contours we emphasize ROIs with at least 30 green pixels used to emphasize the influence of saturation (see below).

For each recording, we filter the ROI traces at 1s (*middle*) and 10s (*right*) to separate the trace into slow and fast component. For each ROI we then randomly choose 100 values of the slow component together with the variance of the fast component from a window around the same timepoint, with window size the same as the timescale. (Note the log-log scale of the axes, so that for a dependence of type $y = kx^n$, the apparent offset in the log-log plot is defined by slope of the dependence k, and the apparent slope in the plot by the exponent n.)

In agreement with our assumptions, the variances and the means are linearly dependent ($n = 1$), and in the case of raw photon counts, the dependence is exactly 1 (solid diagonal line $\sigma^2 = \mu$). In the standard mode with non-unit gain, the dependence is still linear, yet with a slope larger than one (dashed orange line). Points above the bulk in this view are due to windows with larger variance, and presumably connected with activity (at the appropriate timescale). Points below the bulk are due to undervariate windows. They are concentrated at high values and are due to saturated pixels. In the lower right plot we emphasize this fact by showing the points from saturated ROIs in red.

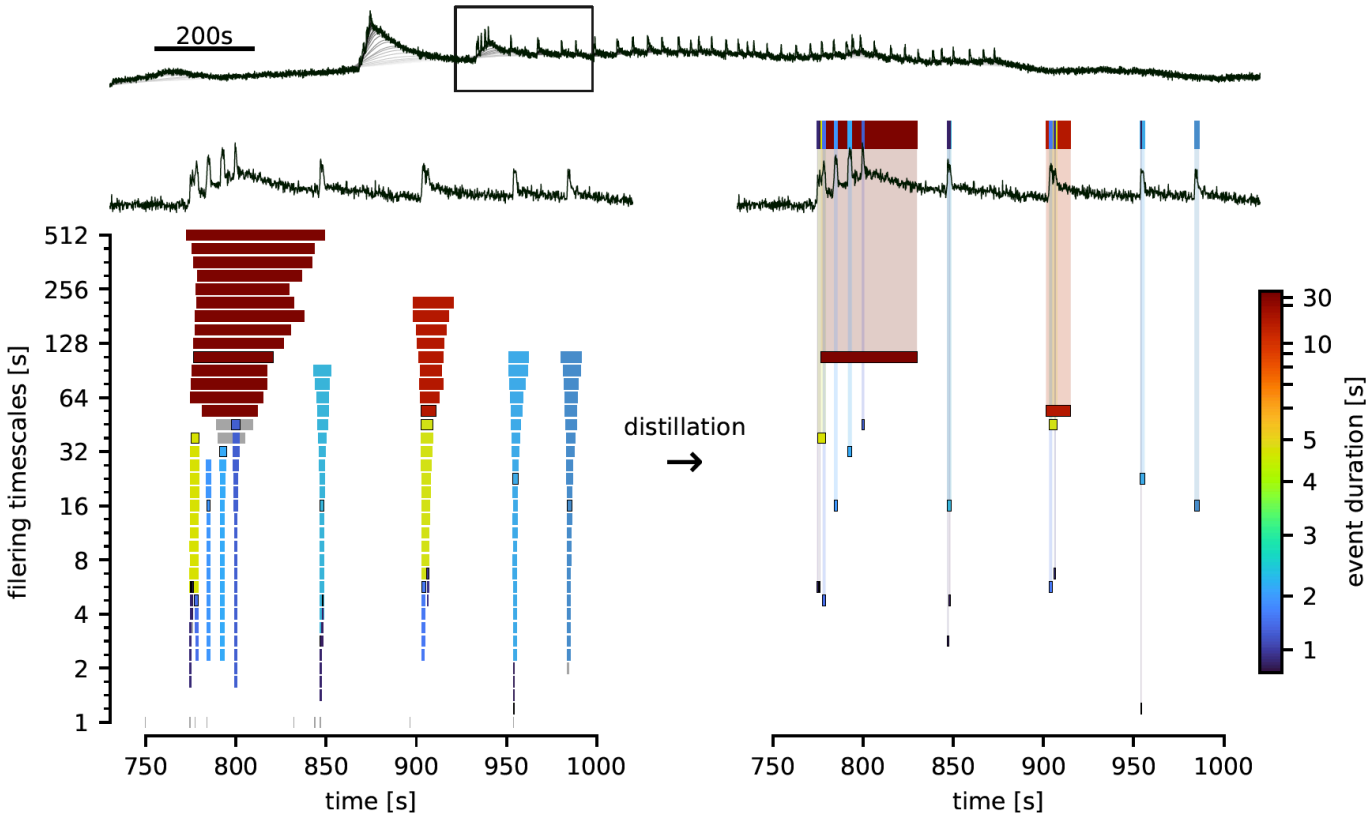

Figure S9-4. **A**, Example of a trace (black) and slow components in sequential filtering (shades of gray). **B**, Close-up view of the indicated small region from (A) and a representation of all candidate events in that region detected through sequential filtering. Each bar represents an event. Vertical position corresponds to the timescale at which the event was detected, the horizontal boundaries correspond to beginning and end time. In grey we show events that are deemed false positives, because they are detected at too few filtering timescales. Others events belong to groups of similar events which are then considered real; we show a boundary around the bar of the event closest to the one finally distilled. It's time boundaries are set to median of the whole group, and the color indicates its halfwidth. **C**, Distillation greatly removes redundancies and false positive candidates. Only robust events are selected for further analysis (see text for details). In the top part we represent the distilled events at single height, in a more compact view. We choose a color code (mapping to a hill curve) which is nearly linear up to a few seconds, to emphasize the color difference at the timescales most interesting for our analysis.

Video Figure 1.
Video Figure 2.
Video Figure 3.
Video Figure 4.
Video Figure 5.
Video Figure 6.
Video Figure 7.

Acknowledgments

MSR receives grants by the Austrian Science Fund/Fonds zur Förderung der Wissenschaftlichen Forschung (bilateral grants I3562-B27 and I4319-B30). MSR, AS and DK further received financial support from the Slovenian Research Agency

(research core funding program P3-0396 and projects N3-0048, N3-0133 and J3-9289). JDJ receives grants from CIHR and Diabetes Canada.

References

1. C. Ammala, K. Bokvist, O. Larsson, P. O. Berggren, and P. Rorsman. Demonstration of a novel apamin-insensitive calcium-activated k+ channel in mouse pancreatic b cells. *Pflugers Arch*, 422(5):443–8, 1993.

2. C. Ammala, O. Larsson, P. O. Berggren, K. Bokvist, L. Juntti-Berggren, H. Kindmark, and P. Rorsman. Inositol trisphosphate-dependent periodic activation of a ca(2+)-activated k+ conductance in glucose-stimulated pancreatic beta-cells. *Nature*, 353(6347):849–52, 1991.

3. P. Arkhammar, T. Nilsson, P. Rorsman, and O. Berggrens. The journal of biological chemistry inhibition of atp-regulated k+ channels precedes depolarization-induced increase in cytoplasmic free ca2+ concentration in pancreatic beta cells. *THE JOURNAL OF BIOLOGICAL CHEMISTRY*, 1987.

4. F. M. Ashcroft and P. Rorsman. Electrophysiology of the pancreatic beta-cell. *Prog Biophys Mol Biol*, 54(2):87–143, 1989.

5. M. C. Beauvois, A. Arredouani, J. C. Jonas, J. F. Rolland, F. Schuit, J. C. Henquin, and P. Gilon. Atypical ca2+-induced ca2+ release from a sarco-endoplasmic reticulum ca2+-atpase 3-dependent ca2+ pool in mouse pancreatic beta-cells. *J Physiol*, 559(Pt 1):141–56, 2004.

6. M. J. Berridge. The am and fm of calcium signalling. *Nature*, 386(6627):759–760, 1997.

7. M. J. Berridge. Unlocking the secrets of cell signaling. *Annu Rev Physiol*, 2004.

8. M. J. Berridge, P. Lipp, and M. D. Bootman. The versatility and universality of calcium signalling. *Nature Reviews Molecular Cell Biology*, 1(1):11–21, 2000.

9. J. D. Bruton, R. Lemmens, C. L. Shi, S. Persson-Sjogren, H. Westerblad, M. Ahmed, N. J. Pyne, M. Frame, B. L. Furman, and M. S. Islam. Ryanodine receptors of pancreatic beta-cells mediate a distinct context-dependent signal for insulin secretion. *Faseb j*, 17(2):301–3, 2003.

10. A. Caicedo. Paracrine and autocrine interactions in the human islet: more than meets the eye. *Semin Cell Dev Biol*, 24(1):11–21, 2013.

11. J. Chen, H. Cha-Molstad, A. Szabo, and A. Shalev. Diabetes induces and calcium channel blockers prevent cardiac expression of proapoptotic thioredoxin-interacting protein. *Am J Physiol Endocrinol Metab*, 296(5):E1133–9, 2009.

12. W. Chen, R. Wang, B. Chen, X. Zhong, H. Kong, Y. Bai, Q. Zhou, C. Xie, J. Zhang, A. Guo, X. Tian, P. P. Jones, M. L. O'Mara, Y. Liu, T. Mi, L. Zhang, J. Bolstad, L. Semeniuk, H. Cheng, J. Zhang, J. Chen, D. P. Tieleman, A. M. Gillis, H. J. Duff, M. Fill, L.-S. Song, and S. R. W. Chen. The ryanodine receptor store-sensing gate controls ca2+ waves and ca2+-triggered arrhythmias. *Nature Medicine*, 20(2):184–192, 2014.

13. Z. Chen, Z. Li, G. Peng, X. Chen, W. Yin, M. I. Kotlikoff, Z.-Q. Yuan, and G. Ji. Extracellular atp-induced nuclear ca2+ transient is mediated by inositol 1,4,5-trisphosphate receptors in mouse pancreatic beta-cells. *Biochemical and Biophysical Research Communications*, 382(2):381–384, 2009.

14. J. Dolenšek, M. S. Rupnik, and A. Stožer. Structural similarities and differences between the human and the mouse pancreas. *Islets*, 7(1):e1024405–e1024405, 2015.

15. G. Drews, P. Krippeit-Drews, and M. Dufer. Electrophysiology of islet cells. *Adv Exp Med Biol*, 654:115–63, 2010.

16. O. Dyachok and E. Gylfe. Ca(2+)-induced ca(2+) release via inositol 1,4,5-trisphosphate receptors is amplified by protein kinase a and triggers exocytosis in pancreatic beta-cells. *J Biol Chem*, 279(44):45455–61, 2004.

17. O. Dyachok, G. Tufveson, and E. Gylfe. Ca2+-induced ca2+ release by activation of inositol 1,4,5-trisphosphate receptors in primary pancreatic beta-cells. *Cell Calcium*, 36(1):1–9, 2004.

18. T. T. Fischer and B. E. Ehrlich. Wolfram syndrome: a monogenic model for diabetes mellitus and neurodegeneration. *Current Opinion in Physiology*, 17:115–123, 2020.

19. S. G. Fonseca, J. Gromada, and F. Urano. Endoplasmic reticulum stress and pancreatic beta-cell death. *Trends in Endocrinology & Metabolism*, 2011.

20. P. Gilon, H. Y. Chae, G. A. Rutter, and M. A. Ravier. Calcium signaling in pancreatic beta-cells in health and in type 2 diabetes. *Cell Calcium*, 56(5):340–61, 2014.

21. P. Gilon and J. C. Henquin. Influence of membrane potential changes on cytoplasmic ca2+ concentration in an electrically excitable cell, the insulin-secreting pancreatic b-cell. *Journal of Biological Chemistry*, 267(29):20713–20720, 1992.

22. P. Gilon and J. C. Henquin. Mechanisms and physiological significance of the cholinergic control of pancreatic beta-cell function. *Endocr Rev*, 22(5):565–604, 2001.

23. A. Giovannucci, J. Friedrich, P. Gunn, J. Kalfon, B. L. Brown, S. A. Koay, J. Taxidis, F. Najafi, J. L. Gauthier, P. Zhou, B. S. Khakh, D. W. Tank, D. B. Chklovskii, and E. A. Pnevmatikakis. Caiman an open source tool for scalable calcium imaging data analysis. *eLife*, 8, 2019.

24. S. O. Gopel. Activation of ca2+-dependent k+ channels contributes to rhythmic firing of action potentials in mouse pancreatic beta cells. *The Journal of General Physiology*, 114(6):759–770, 1999.

25. M. Gosak, A. Stožer, R. Markovic, J. Dolenšek, M. Perc, M. S. Rupnik, and M. Marhl. Critical and supercritical spatiotemporal calcium dynamics in beta cells. *Frontiers in Physiology*, 8(DEC), 2017.

26. T. Guo, D. Gillespie, and M. Fill. Ryanodine receptor current amplitude controls ca2+ sparks in cardiac muscle. *Circulation research*, 111(1):28–36, 2012.

27. S. Göpel, T. Kanno, S. Barg, J. Galvanovskis, and P. Rorsman. Voltage-gated and resting membrane currents recorded from b-cells in intact mouse pancreatic islets. *The Journal of Physiology*, 521(3):717–728, 1999.

28. R. E. Hagar* and B. E. Ehrlich. Regulation of the type iii insp3 receptor and its role in beta cell function. *Cellular and Molecular Life Sciences*, 57(13):1938–1949, 2000.

29. C. R. Harris, K. J. Millman, S. J. Van Der Walt, R. Gommers, P. Virtanen, D. Cournapeau, E. Wieser, J. Taylor, S. Berg, N. J. Smith, R. Kern, M. Picus, S. Hoyer, M. H. Van Kerkwijk, M. Brett, A. Haldane, J. F. Del Río, M. Wiebe, P. Peterson, P. Gérard-Marchant, K. Sheppard, T. Reddy, W. Weckesser, H. Abbasi, C. Gohlke, and T. E. Oliphant. Array programming with numpy. *Nature*, 585(7825):357–362, 2020.

30. M. J. Henderson, K. A. Trychta, S.-M. Yang, S. Bäck, A. Yasgar, E. S. Wires, C. Danchik, X. Yan, H. Yano, L. Shi, K.-J. Wu, A. Q. Wang, D. Tao, G. Zahoránszky-Kőhalmi, X. Hu, X. Xu, D. Maloney, A. V. Zakharov, G. Rai, F. Urano, M. Airavaara, O. Gavrilova, A. Jadhav, Y. Wang, A. Simeonov, and B. K. Harvey. A target-agnostic screen identifies approved drugs to stabilize the endoplasmic reticulum-resident proteome. *Cell Reports*, 35(4), 2021.

31. J. C. Henquin. Glucose-induced insulin secretion in isolated human islets: does it truly reflect beta-cell function in vivo? *Mol Metab*, page 101212, 2021.

32. J. C. Henquin and H. P. Meissner. Significance of ionic fluxes and changes in membrane potential for stimulus-secretion coupling in pancreatic b-cells. *Experientia*, 40(10):1043–1052, 1984.

33. G. G. Holz, C. A. Leech, R. S. Heller, M. Castonguay, and J. F. Habener. camp-dependent mobilization of intracellular ca2+ stores by activation of ryanodine receptors in pancreatic beta-cells. a ca2+ signaling system stimulated by the insulinotropic hormone glucagon-like peptide-1-(7-37). *J Biol Chem*, 274(20):14147–56, 1999.

34. M. S. Islam. The ryanodine receptor calcium channel of beta-cells: Molecular regulation and physiological significance. *Diabetes*, 2002.

35. M. S. Islam, P. Rorsman, and P.-O. Berggren. Ca2+ -induced ca2+ release in insulin-secreting cells. *FEBS Letters*, 296(3):287–291, 1992.

36. J. D. Johnson, S. Kuang, S. Misler, and K. S. Polonsky. Ryanodine receptors in human pancreatic beta cells: localization and effects on insulin secretion. *The FASEB journal : official publication of the Federation of American Societies for Experimental Biology*, 2004.

37. G. Kang, O. G. Chepurny, M. J. Rindler, L. Collis, Z. Chepurny, W.-h. Li, M. Harbeck, M. W. Roe, and G. G. Holz. A camp and ca 2+ coincidence detector in support of ca 2+ -induced ca 2+ release in mouse pancreatic beta cells. *The Journal of Physiology*, 566(1):173–188, 2005.

38. C. Klec, C. T. Madreiter-Sokolowski, S. Stryeck, V. Sachdev, M. Duta-Mare, B. Gottschalk, M. R. Depaoli, R. Rost, J. Hay, M. Waldeck-Weiermair, D. Kratky, T. Madl, R. Malli, and W. F. Graier. Glycogen synthase kinase 3 beta controls presenilin-1-mediated endoplasmic reticulum ca(2)(+) leak directed to mitochondria in pancreatic islets and beta-cells. *Cell Physiol Biochem*, 52(1):57–75, 2019.

39. G. Larsson-Nyrén, J. Sehlin, P. Rorsman, and E. Renström. Perchlorate stimulates insulin secretion by shifting the gating of l-type ca2+ currents in mouse pancreatic b-cells towards negative potentials. *Pflügers Archiv*, 441(5):587–595, 2001.

40. J. T. C. Lee, I. Shanina, Y. N. Chu, M. S. Horwitz, and J. D. Johnson. Carbamazepine, a beta-cell protecting drug, reduces type 1 diabetes incidence in nod mice. *Scientific Reports*, 8(1), 2018.

41. A. Lombardi and Y. Tomer. Interferon alpha impairs insulin production in human beta cells via endoplasmic reticulum stress. *Journal of Autoimmunity*, 80:48–55, 2017.

42. D. S. Luciani, K. S. Gwiazda, T. L. Yang, T. B. Kalynyak, Y. Bychkivska, M. H. Frey, K. D. Jeffrey, A. V. Sampaio, T. M. Underhill, and J. D. Johnson. Roles of ip3r and ryr ca2+ channels in endoplasmic reticulum stress and beta-cell death. *Diabetes*, 58(2):422–32, 2009.

43. A. Marciniak, C. M. Cohrs, V. Tsata, J. A. Chouinard, C. Selck, J. Stertmann, S. Reichelt, T. Rose, F. Ehehalt, J. Weitz, M. Solimena, M. Slak Rupnik, and S. Speier. Using pancreas tissue slices for in situ studies of islet of langerhans and acinar cell biology. *Nature Protocols*, 9(12):2809–2822, 2014.

44. R. Markovič, A. Stožer, M. Gosak, J. Dolenšek, M. Marhl, and M. S. Rupnik. Progressive glucose stimulation of islet beta cells reveals a transition from segregated to integrated modular functional connectivity patterns. *Scientific Reports*, 5:7845–7845, 2015.

45. J. Marquard, S. Otter, A. Welters, A. Stirban, A. Fischer, J. Eglinger, D. Herebian, O. Kletke, M. S. Klemen, A. Stozer, S. Wnendt, L. Piemonti, M. Kohler, J. Ferrer, B. Thorens, F. Schliess, M. S. Rupnik, T. Heise, P. O. Berggren, N. Klocker, T. Meissner, E. Mayatepek, D. Eberhard, M. Kragl, and E. Lammert. Characterization of pancreatic nmda receptors as possible drug targets for diabetes treatment. *Nat Med*, 21(4):363–72, 2015.

46. M. Michalak, J. M. Robert Parker, and M. Opas. Ca2+ signaling and calcium binding chaperones of the endoplasmic reticulum. *Cell Calcium*, 32(5-6):269–278, 2002.

47. M. Montero, M. Brini, R. Marsault, J. Alvarez, R. Sitia, T. Pozzan, and R. Rizzuto. Monitoring dynamic changes in free ca2+ concentration in the endoplasmic reticulum of intact cells. *The EMBO Journal*, 14(22):5467–5475, 1995.

48. M. A. Ostuni, P. Hermand, E. Saindoy, N. Guillou, J. Guellec, A. Coens, C. Hattab, E. Desuzinges-Mandon, A. Jawhari, S. Iatmanen-Harbi, O. Lequin, P. Fuchs, J. J. Lacapere, C. Combadiere, F. Pincet, and P. Deterre. Cx3cl1 homo-oligomerization drives cell-to-cell adherence. *Sci Rep*, 10(1):9069, 2020.

49. F. Ovalle, T. Grimes, G. Xu, A. J. Patel, T. B. Grayson, L. A. Thielen, P. Li, and A. Shalev. Verapamil and beta cell function in adults with recent-onset type 1 diabetes. *Nature Medicine*, 24(8):1108–1112, 2018.

50. E. R. Pearson, I. Flechtner, P. R. Njølstad, M. T. Malecki, S. E. Flanagan, B. Larkin, F. M. Ashcroft, I. Klimes, E. Codner, V. Iotova, A. S. Slingerland, J. Shield, J.-J. Robert, J. J. Holst, P. M. Clark, S. Ellard, O. Søvik, M. Polak,

and A. T. Hattersley. Switching from insulin to oral sulfonylureas in patients with diabetes due to kir6.2 mutations. *New England Journal of Medicine*, 355(5):467–477, 2006.

51. M. A. Ravier, D. Daro, L. P. Roma, J. C. Jonas, R. Cheng-Xue, F. C. Schuit, and P. Gilon. Mechanisms of control of the free ca2+ concentration in the endoplasmic reticulum of mouse pancreatic beta-cells: interplay with cell metabolism and [ca2+]c and role of serca2b and serca3. *Diabetes*, 60(10):2533–45, 2011.

52. M. A. Ravier, M. Güldenagel, A. Charollais, A. Gjinovci, D. Caille, G. Söhl, C. B. Wollheim, K. Willecke, J.-C. Henquin, and P. Meda. Loss of connexin36 channels alters beta-cell coupling, islet synchronization of glucose-induced ca2+ and insulin oscillations, and basal insulin release. *Diabetes*, 54(6):1798–1807, 2005.

53. M. W. Roe, M. E. Lancaster, R. J. Mertz, r. Worley, J. F., and I. D. Dukes. Voltage-dependent intracellular calcium release from mouse islets stimulated by glucose. *J Biol Chem*, 268(14):9953–6, 1993.

54. P. Rorsman and F. M. Ashcroft. Pancreatic β-cell electrical activity and insulin secretion: Of mice and men. *Physiological Reviews*, 98(1):117–214, 2018.

55. J. V. Sanchez-Andres, R. Pomares, and W. J. Malaisse. Adaptive short-term associative conditioning in the pancreatic β-cell. *Physiological Reports*, 8(6):e14403, 2020.

56. G. Santulli, R. Nakashima, Q. Yuan, and A. R. Marks. Intracellular calcium release channels: an update. *J Physiol*, 595(10):3041–3051, 2017.

57. G. Santulli, G. Pagano, C. Sardu, W. Xie, S. Reiken, S. L. D'Ascia, M. Cannone, N. Marziliano, B. Trimarco, T. A. Guise, A. Lacampagne, and A. R. Marks. Calcium release channel ryr2 regulates insulin release and glucose homeostasis. *Journal of Clinical Investigation*, 2015.

58. V. Schulla, E. Renström, R. Feil, S. Feil, I. Franklin, A. Gjinovci, X. J. Jing, D. Laux, I. Lundquist, M. A. Magnuson, S. Obermüller, C. S. Olofsson, A. Salehi, A. Wendt, N. Klugbauer, C. B. Wollheim, P. Rorsman, and F. Hofmann. Impaired insulin secretion and glucose tolerance in β cell-selective cav1.2 ca2+ channel null mice. *EMBO Journal*, 22(15):3844–3854, 2003.

59. M. Skelin Klemen, J. Dolenšek, M. Slak Rupnik, and A. Stožer. The triggering pathway to insulin secretion: Functional similarities and differences between the human and the mouse beta cells and their translational relevance. *Islets*, pages 00–00, 2017.

60. R. Sladek, G. Rocheleau, J. Rung, C. Dina, L. Shen, D. Serre, P. Boutin, D. Vincent, A. Belisle, S. Hadjadj, B. Balkau, B. Heude, G. Charpentier, T. J. Hudson, A. Montpetit, A. V. Pshezhetsky, M. Prentki, B. I. Posner, D. J. Balding, D. Meyre, C. Polychronakos, and P. Froguel. A genome-wide association study identifies novel risk loci for type 2 diabetes. *Nature*, 445(7130):881–5, 2007.

61. N. Sluga, S. Postić, S. Sarikas, Y.-C. Huang, A. Stožer, and M. Slak Rupnik. Dual Mode of Action of Acetylcholine on Cytosolic Calcium Oscillations in Pancreatic Beta and Acinar Cells in Situ. *Preprints*, May 2021.

62. S. Speier, A. Gjinovci, A. Charollais, P. Meda, and M. Rupnik. Cx36-mediated coupling reduces β-cell heterogeneity, confines the stimulating glucose concentration range, and affects insulin release kinetics. *Diabetes*, 56(4):1078–1086, 2007.

63. S. Speier and M. Rupnik. A novel approach to in situ characterization of pancreatic beta-cells. *Pflügers Archiv European Journal of Physiology*, 446(5):553–558, 2003.

64. S. Speier, S. B. Yang, K. Sroka, T. Rose, and M. Rupnik. Katp-channels in beta-cells in tissue slices are directly modulated by millimolar atp. *Molecular and Cellular Endocrinology*, 230(1-2):51–58, 2005.

65. A. Stožer, J. Dolenšek, and M. S. Rupnik. Glucose-stimulated calcium dynamics in islets of langerhans in acute mouse pancreas tissue slices. *PLoS ONE*, 8(1), 2013.

66. A. Stožer, R. Markovič, J. Dolenšek, M. Perc, M. Marhl, M. Slak Rupnik, and M. Gosak. Heterogeneity and delayed activation as hallmarks of self-organization and criticality in excitable tissue. *Frontiers in Physiology*, 10, 2019.

67. S. Takasawa, M. Kuroki, K. Nata, N. Noguchi, T. Ikeda, A. Yamauchi, H. Ota, A. Itaya-Hironaka, S. Sakuramoto-Tsuchida, I. Takahashi, T. Yoshikawa, T. Shimosegawa, and H. Okamoto. A novel ryanodine receptor expressed in pancreatic islets by alternative splicing from type 2 ryanodine receptor gene. *Biochemical and Biophysical Research Communications*, 2010.

68. N. A. Tamarina, Y. Wang, L. Mariotto, A. Kuznetsov, C. Bond, J. Adelman, and L. H. Philipson. Small-conductance calcium-activated k+ channels are expressed in pancreatic islets and regulate glucose responses. *Diabetes*, 52(8):2000–2006, 2003.

69. A. Tengholm, B. Hellman, and E. Gylfe. The endoplasmic reticulum is a glucose-modulated high-affinity sink for ca2+ in mouse pancreatic beta-cells. *J Physiol*, 530(Pt 3):533–40, 2001.

70. X. Tong, T. Kono, E. K. Anderson-Baucum, W. Yamamoto, P. Gilon, D. Lebeche, R. N. Day, G. E. Shull, and C. Evans-Molina. Serca2 deficiency impairs pancreatic beta-cell function in response to diet-induced obesity. *Diabetes*, 65(10):3039–3052, 2016.

71. F. Van Petegem. Ryanodine receptors: structure and function. *J Biol Chem*, 287(38):31624–32, 2012.

72. C. B. Wollheim and G. W. Sharp. Regulation of insulin release by calcium. *Physiol Rev*, 61(4):914–73, 1981.

73. r. Worley, J. F., M. S. McIntyre, B. Spencer, R. J. Mertz, M. W. Roe, and I. D. Dukes. Endoplasmic reticulum calcium store regulates membrane potential in mouse islet beta-cells. *J Biol Chem*, 269(20):14359–62, 1994.

74. W. R. Yamamoto, R. N. Bone, P. Sohn, F. Syed, C. A. Reissaus, A. L. Mosley, A. B. Wijeratne, J. D. True, X. Tong, T. Kono, and C. Evans-Molina. Endoplasmic reticulum stress alters ryanodine receptor function in the murine pancreatic β cell. *Journal of Biological Chemistry*, 294(1):168–181, 2019.

75. Y. H. C. Yang, Y. Y. Vilin, M. Roberge, H. T. Kurata, and J. D. Johnson. Multiparameter screening reveals a role for na+ channels in cytokine-induced beta cell death. *Molecular Endocrinology*, 28(3):406–417, 2014.

76. B. J. Zunkler, S. Lenzen, K. Manner, U. Panten, and G. Trube. Concentration-dependent effects of tolbutamide, meglitinide, glipizide, glibenclamide and diazoxide on atp-regulated k+ currents in pancreatic b-cells. *Naunyn Schmiedebergs Arch Pharmacol*, 337(2):225–30, 1988.